Received: 24 June 2024 | Revised: 22 February 2025 | Accepted: 26 February 2025

DOI: 10.1002/qj.4974

Quarterly Journal of the Royal Meteorological Society RMetS

RESEARCH ARTICLE

Regional to large-scale mechanisms controlling intraseasonal variability of low-level clouds in Western Equatorial Africa

Vincent Moron[1] | **Pierre Camberlin**[2] | **Nathalie Philippon**[3] | **Andreas H. Fink**[4] | **Peter Knippertz**[4]

[1]Aix Marseille Univ, CNRS, IRD, INRAE, CEREGE, Aix-en-Provence, France

[2]Biogeosciences, University of Burgundy, Dijon, France

[3]IGE, Grenoble-Alpes University, Grenoble, France

[4]KIT, Karlsruhe, Germany

Correspondence
Vincent Moron, Department of Geography, Planning and Environment, Aix-Marseille University, BP80, 13545 Aix en Provence, France.
Email: moron@cerege.fr

Funding information
Deutsche Forschungsgemeinschaft, Grant/Award Number: DFG FI 786/5-1; Agence Nationale de la Recherche, Grant/Award Number: ANR-19-CE01-0021

Abstract

The intraseasonal variability (ISV) of the stratiform cloud cover over Western Equatorial Africa (WEA) is analysed during the dry season (June–September, JJAS 1971–2019). Each JJAS daily sequence of a regional-scale index of the stratiform cloud cover could be assimilated as a red-noise process, without any significant recurrent periodicities. At local scale, cloudier conditions than usual are preceded by and synchronised with sustained easterly wind and warm anomalies near the top (850 hPa) and above the stratiform cloud deck, indicating higher stability. Anomalous easterlies or northeasterlies bring also anomalously moist air from either the Congo Basin or the West-African rainbelt region to WEA. At low levels (<850 hPa), there is a clear switch between antecedent warm easterlies and synchronous cool and dry westerlies from the cold-tongue area over the equatorial Atlantic. This switch may reflect a negative feedback loop, operating on a short time-scale (i.e., ~3–5 days) and involving low-level thermal and geopotential gradients, zonal winds between the cold-tongue area and the Congo Basin, as well as the deep convection over the latter region. Kelvin waves appear to be a possible trigger of this loop, which could be sustained internally. Another main process operates at longer time-scales (i.e., ~6–10 days) and involves a near-standing Rossby wave over the South Atlantic and adjacent southern Africa. A ridge over the central South Atlantic and downstream trough over southern Africa lead to an overall strengthening of the St. Helena high, and increased thermal and geopotential gradients between the southeast South Atlantic and southern Africa. The ridge–trough couple is also related to an anomalous warming over equatorial Africa in the middle troposphere associated with increased lower-tropospheric stability over WEA a few days later. All these mechanisms contribute to the knowledge regarding the intraseasonal atmospheric variations over equatorial Africa during boreal summer.

KEYWORDS

Kelvin wave, lower-tropospheric stability, Rossby wave, South Atlantic, tropical Africa

1 | INTRODUCTION

Western Equatorial Africa (WEA) exhibits an almost unique seasonal character across the whole tropical zone, namely a long June–September (JJAS) almost absolute dry season combined with a compact stratiform cloud cover (Dommo et al., 2018; Philippon et al., 2016, 2019) limiting both direct solar radiation and evapotranspiration, thus leading to very specific climatological conditions. This combination of dry conditions and overcast skies, rather common over the oceanic eastern edges of subtropical anticyclones (Eastman et al., 2011; Wood, 2012) is here not strictly restricted to a narrow coastal plain, as usually observed along the tropical and subtropical cold ocean currents, but penetrates more than 500 km inland and thus covers the coastal plains, as well as the low mountain ranges in the coastal hinterland and inland plateaus (i.e., Mts de Cristal, Massif de Chaillu, Batéké Plateaus) (Champagne et al., 2023; Dommo et al., 2018; Magnan et al., 2024) of the southwestern Republic of Congo (RC), most of Gabon and southern Cameroon. The most persistent and thick low-level cloud cover is observed on the windward, i.e., western, side of the low mountain ranges of WEA, while it disappears rather fast on their leeward slopes, roughly east of 14° E toward the Congo basin (Champagne et al., 2023).

The seasonality of the stratiform cloud cover (Champagne et al., 2023; Dommo et al., 2018) is strongly phase-locked to the development of the equatorial upwelling over the Atlantic cold-tongue area mostly between 5° S and the equator, and to the regional-scale atmospheric system related to the boreal summer West-African monsoon, including the northward migration of the Intertropical Convergence Zone (ITCZ), subsidence over the equatorial upwelling and increased southerly low-level flow over most of the southern and equatorial Atlantic (Gu & Adler, 2004; Janicot et al., 2011). Note that, even though being a relative dry season (Hart et al., 2019; Washington et al., 2013), the JJAS period, over the Congo Basin is related to outbreaks of deep convection and significant rainfall roughly east of 15–20° E (Hart et al., 2019; Washington et al., 2013).

The stratiform cloud deck is also strongly modulated at the diurnal scale with low-level cloud fraction peaking between late night and morning and decreasing during the afternoon and early nights (Champagne et al., 2023; Dommo et al., 2018, 2022; Magnan et al., 2024). Moron et al. (2023) show that the afternoon decrease of the low-cloud fraction (LCF) is frequently combined with a transition from stratiform clouds to more or less fragmented cumulus genus. Dommo et al. (2022) associate the diurnal changes in ERA5 low clouds over WEA to a complex mixture of processes, with their formation in early night mostly due to the combination of radiative cooling with horizontal advection of moisture and convergence in the boundary layer when the low-level westerlies are the fastest. They also related fast low-level westerlies with turbulent upward mixing motion below and in the cloud deck. The partial or complete lysis of the stratiform cloud deck from noon is mostly due to increased heat fluxes from the surface and deepening of the boundary layer, decreasing the relative humidity in the boundary layer (Dommo et al., 2022; Lohou et al., 2020).

The interannual variations of the stratiform cloud cover over WEA mostly involve the equatorial Atlantic sea surface temperatures (SST), but also the El Niño–Southern Oscillation (ENSO) phenomenon (Moron et al., 2023). The SST variations in the eastern equatorial and SE Atlantic play a dominant role. Anomalously cold SE Atlantic SST enhance the low-level thermal and geopotential zonal gradients with the Congo Basin, and promote anomalous advection of cool air, increasing the in-situ lower-tropospheric stability (LTS). Anomalously cold SST anomalies over the equatorial Atlantic are also related to a shallow meridional overturning, combining anomalous ascent around 5–7° N and anomalous subsidence over the equatorial Atlantic and nearby WEA (Moron et al., 2023). Remote warm ENSO events also impact the stratiform cloud cover at interannual time-scales, due to sustained warm and easterly anomalies in the middle troposphere, increasing LTS from above.

The main objective of this study is to analyse the intraseasonal variations (ISV) of the stratiform cloud cover over WEA. We used the same database of 26 synoptic stations created in Champagne et al. (2023) mostly from the Extended Edited Synoptic Cloud Report Archive (EECRA) database (Eastman et al., 2011; Hahn et al., 2003) and already used in Moron et al. (2023). The observed LCF from the stations is combined with ERA5 LCF to produce a single index depicting the LCF intraseasonal variation over the cloudiest area of WEA. Section 2 describes the data used in this study. Section 3 details the analysis of the ISV, including an exploratory analysis of the role of the coupled convective equatorial waves. Section 4 discusses the main findings while Section 5 concludes the paper.

2 | DATA AND METHODS

2.1 | LCF and other oceano-atmospheric data

Analyses are restricted to the main cloudy season, i.e., June–September (Dommo et al., 2018; Magnan et al., 2024; Moron et al., 2023; Philippon et al., 2016) and the 1971–2019 period (i.e., 49 JJAS seasons). Regarding the

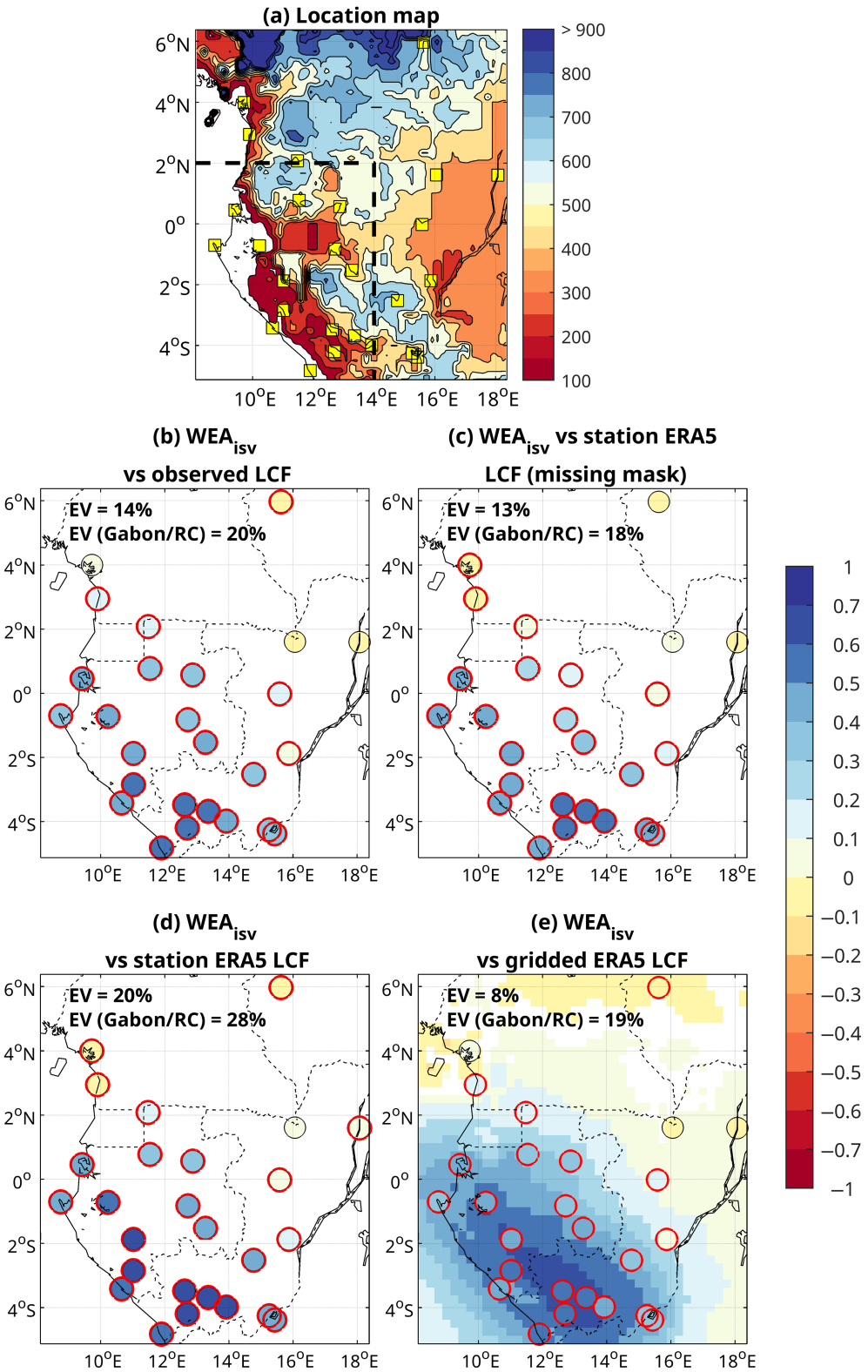

FIGURE 1 (a) Location map with the 26 stations as yellow squares superimposed on the topography in meters above sea level. Correlations between WEA_{isv} and (b) observed LCF, (c) ERA5 LCF at the same location as stations with the same missing entries, (d) ERA5 LCF at the same location as stations without missing entries, (e) gridded ERA5 LCF (shadings) and observed LCF (dots). All correlations are computed for the period JJAS 1971–2019. The red circles (and shadings on panel e) indicate significant correlations at the two-sided 95% level according to a random-phase test. EV is the percentage of explained variance (spatial average of squared correlations) across the 15 stations chosen to compute WEA_{isv} (in the area bounded by a black dashed line on panel a).

observed LCF, we used the same dataset of 26 synoptic stations, updating the EECRA from Ships and Land Stations Over the Globe database (Hahn et al., 2003), as in Champagne et al. (2023) and Moron et al. (2023) (Figure 1a). The atmospheric variables (temperature [T], zonal [u] and meridional [v] components of the wind, geopotential height [z], vertical velocity [w], and specific humidity [q]) and SST are all extracted from ERA5 (Hersbach et al., 2020) at the native spatial resolution (0.25°) and three-hourly time-scale (from 0000 UTC) to match the temporal resolution of the observed LCF (Aellig et al., 2022). We focus on the 1000, 925, 850 and

700 hPa levels, the third level being close to the usual top of the stratiform cloud deck over WEA (Champagne et al., 2023; Dommo et al., 2018), but also explore the geopotential height at 300 hPa to analyse the possible role of extratropical Rossby waves.

2.2 | Extraction of intraseasonal variability

All data are processed in exactly the same way to extract the intraseasonal variability. First, for each variable, the daily climatology has been computed and removed to get deseasonalised anomalies still including the interannual variability. Then, the yearly JJAS mean has been computed from the deseasonalised anomalies and removed to get the ISV only. As a consequence, the intraseasonal variability (ISV) defined here contains all variations beyond two days, thus including synoptic-scale variability and the Madden–Julian oscillation (i.e., 20–60 days). For LCF data which are at a three-hourly resolution, a three-hourly climatological mean is first computed and all three-hourly values are expressed as anomalies. Then, these three-hourly LCF anomalies are averaged at daily time-scale to get daily anomalies.

2.3 | Definition of the intraseasonal variations of the low-cloud cover

The index used for studying WEA LCF intraseasonal variability is constructed by blending observed and ERA5 data. The aim is to tackle the uncertainties due to the limited available entries, such as the low number of available stations which are also unevenly distributed (Figure 1), and the possible bias related to the uneven sampling of the diurnal cycle (Champagne et al., 2023; Dommo et al., 2018). As explained in Moron et al. (2023), the ERA5 LCF is prefiltered using the convective rainfall to filter out the bases of cumulonimbus. This method improves the matching between observed and ERA5 LCF data.

The amount of missing data in the three-hourly LCF data at the 26 stations is huge (55%), especially during the night (69%–71% of missing entries between 2100 UTC and 0300 UTC vs 40% of missing entries at 1200 UTC; Aellig et al., 2022). The uncertainties related to the space–time sampling, combined with the intrinsic difficulty to observe low-cloud cover and its space–time variations, introduce random noise in the data. This is especially true at a daily time-scale, since a monthly or a seasonal average, or by definition any climatological mean, tends to partially cancel out inconsistent variations across time. Having also more three-hourly data at daytime than at nighttime may potentially distort the daily average as the diurnal cycle is large: mean LCF peaks between 0300 UTC and 0900 UTC and is minimum at 1500 UTC (Champagne et al., 2023; Dommo et al., 2018, 2022; Magnan et al., 2024; Moron et al., 2023).

A first challenge is thus to extract a robust intraseasonal LCF signal. The accuracy of ERA5 LCF at seasonal and interannual time-scales (Moron et al., 2023) offers the opportunity to evaluate the impact of some uncertainties. We consider two strategies to compute a robust index: (a) the weighted spatial average of the cloudiest area defined as the 15 stations with a mean JJAS daily LCF of at least 4 octas (roughly between 2° N and 6° S and west of 14° E, Figure 1). It is referred to as a standardised anomaly index (SAI – Katz & Glantz, 1986) as the weights are proportional to the average cross-correlations between one station and the others. The variance of the SAI is also adjusted for the variable number of available stations to not bias its variance (Osborn et al. 1997); (b) the first Empirical Orthgonal Function (EOF) mode of all stations obtained by applying a probabilistic algorithm (Verbeek et al., 2002) able to handle sparse matrices with a large number of missing entries.

These two strategies were applied to four different samples: (1) the observed LCF; (2) the ERA5 LCF co-located with the 26 stations and with the same three-hourly missing values as observations; (3) the ERA5 LCF co-located with the 26 stations without missing entries; (4) the ERA5 LCF grid points approximately bounded by the extreme latitudes and longitudes of the observed network. By comparing (1) with (2–4), we can estimate the overall accuracy of ERA5 at the intraseasonal time-scale; the comparison between (2) and (3) gives an approximation of the impact of missing entries in time; the comparison between (3) and (4) gives an approximation of the impact of horizontal sampling. The solutions (1) and (4) seem the furthest apart in terms of sampling.

Computing either an SAI or the leading EOF over all the stations/grid points leads to similar variations with correlations of 0.77–0.83 between the two corresponding time series. Note that correlations are always higher than 0.9 when the index (SAI or leading EOF) is restricted to the core cloudiest area (i.e., the 15 cloudiest stations/grid points bounded by the black dashed line in Figure 1a). All correlations are significant at the two-sided 95% level according to a random-phase test (Janicot et al., 1996).

Finally, a hybrid SAI (referred to as WEA_{isv} hereafter) is computed using the observed LCF data at the 15 cloudiest stations concatenated column-wise with the complete ERA5 LCF data at the co-located grid points, so that a total of 30 variables are used (Figure 1a). Note that this index is nearly insensitive to several methodological choices. For instance, WEA_{isv} is correlated at 0.83

with the SAI using the observed LCF at the 15 stations only (solution 1), 0.87 with the SAI using the complete ERA5 LCF data on the 15 co-located grid points with observed stations (solution 3) and 0.80 with the SAI using the complete gridded ERA5 LCF data bounded by the black dashed line in Figure 1a. Moreover, using a filtered annual cycle by a fifth-order recursive Butterworth filter with a cut-off at 1/60 cycle-per-day to estimate the intraseasonal anomalies, leads to a nearly identical WEA_{isv} (correlation = 0.9882 with our initial index on the 5978 available days).

Figure 1b–e shows the correlations between WEA_{isv} and the four different networks. The spatially-consistent pattern covers, as expected, the core of the cloudiest area over most of Gabon and SW of the Republic of Congo (RC) especially windward and over the first hills from the Atlantic coast (Figure 1 of Champagne et al., 2023). The amount of explained variance, given by the spatial average of the squared correlations with WEA_{isv}, is moderate: 18%–28% over the core cloudy area. However this is consistent with the large amount of spatial variance revealed by satellites (Champagne et al., 2023) and again, the uncertainties in the LCF database. WEA_{isv} is used as the reference time series for the analysis of the intraseasonal variability of the WEA stratiform cloud cover in the following analyses.

The fraction of variance of WEA_{isv} due to the 62 frequencies (i.e., including the periods from two days to infinity) has been extracted using a fast Fourier transform processed on each of the 49 JJAS seasons. There are no clear, precise and recurrent periodicities across the seasons (not shown). Figure S1a shows the fraction of variance conveyed by four non-overlapping bandwidths. The largest fraction of variance is usually conveyed by the shortest time-scale of less than seven days (mean = 43.5%, sd = 11.5%) while the second-largest one is usually due to the longest time-scale longer than 21 days (mean = 25.8%, sd = 11.2%). The medium time-scales explain respectively 20.5% (7–14 days, sd = 6.1%) and 10.2% (14–21 days, sd = 5.5%) of the total variance. These fractions do not significantly differ from what is expected for random time series having the same variance and one-order autocorrelation as each JJAS WEA_{isv} time series. The mean relative fractions of total variance across 1000 simulations of 49 red-noise time series of 122 observations equal 44%, 23%, 11%, and 22% respectively for less than seven days, 7–14, 14–21 and more than 21 days bandwidths. The observed fraction is higher than the one expected by chance (at the one-sided 95% level) only in 1980 for less than seven days, in 2008 for 14–21 days and in 1993 and 2003 for more than 21 days (Figure S1a). Considering other bandwidths, such as periods shorter than four or five days, does not change these conclusions (not shown). The variations of WEA_{isv} in JJAS 1980 and 1993 are shown in Figure S1b,c and illustrate the aperiodicity of the LCF ISV.

As WEA_{isv} does exhibit an aperiodic behaviour, we do not restrict our initial analyses to specific ISV bandwidths and prefer to use unfiltered ISV to compute concurrent, then lead–lag correlations (from day −10 to day +3 vs WEA_{isv}) with atmospheric fields. To complete this point of view, we also performed the same lead–lag correlations using low pass 10 days or longer and high pass less than 10 days filtered intraseasonal anomalies. We also explored lagged composite analyses targeted to the occurrence of WEA_{isv} above or below a given threshold at day 0. In these lagged composites (not shown) anomalies are usually symmetrical (negative vs positive), though their absolute amplitude could vary. This justifies the use of a linear approach based on correlations and a linear stepwise regression. The lead–lag correlations are tested for significance using a random-phase test (Ebisuzaki, 1997; Janicot et al., 1996) able to consider the number of degrees of freedom and in particular its loss due to filtering. The first analysis (Figure 3) focuses on time–altitude variations of ERA5 atmospheric parameters over WEA only at a three-hourly time-scale. Then, the following analyses (Figures 4–9) are extended to a regional window including tropical Africa south of 15° N, as well as most of the southern Atlantic, and consider a daily time-scale.

2.4 | Extraction of tropical wave phase and amplitude for WEA

Tropical waves (e.g., Kiladis et al., 2009) are known to modulate JJAS rainfall in the rainy zone located around 12–16° N (e.g., Schlueter et al., 2019a). Tropical waves in their wet phases foster rainfall in that region by causing low-level convergence and moistening, or by enhancing shear in the lower troposphere (Schlueter et al., 2019b). As Kelvin waves, for example, are symmetric about the equator, it is tempting to assume that low-level convergence in their wet phase can also enhance low-level cloudiness in WEA, yet not trigger deep convection due to high vertical stability. Following the methods described in van der Linden et al. (2016) and Schlueter et al. (2019a), the local phase and amplitude of the Madden–Julian Oscillation (MJO), Kelvin waves (KW), Equatorial Rossby waves (ER), Tropical Disturbances (TD), Mixed Gravity Rossby (MRG) Waves, and Eastward Inertio-Gravity waves (EIG) for the period 1979–2019 have been determined. Daily National Oceanic and Atmospheric Administration (NOAA) Outgoing Long-Wave Radiation (OLR) data (Liebmann & Smith, 1996) at 2.5° × 2.5° lon–lat resolution have been frequency-wave-number-filtered (see Schlueter et al., 2019a) over the 5° N–5° S equatorial

belt. As explained in van der Linden et al. (2016), local time-derivative and total OLR are then represented in a phase diagram from which normalised amplitudes of the waves can be inferred. The longitude used in the present study was 12.5° E, centred over the WEA region.

2.5 | A linear stepwise regression model to forecast WEA_{isv}

A statistical model is built in section 4 to synthesise the lagged (from 10 days before WEA_{isv}) and synchronous (lag 0) relationships between WEA_{isv} and a set of 124 atmospheric (= 6 sectors × 4 atmospheric levels between 1000 and 700 hPa × 5 atmospheric variables – T, u, v, w and q + 4 other atmospheric indices, see Fig. 11a) and three SST indices (see Figure 11 below and Section 4). A leave-one-out crossvalidated linear regression model is used (i.e., a full JJAS season is withheld at each turn). The atmospheric and SST indices and WEA_{isv} are standardised at each iteration and the selection of the predictors is made using a 95% significance level with a maximum of 3–10 predictors included in the model. Note that for lags longer than 4–5 days, less predictors can be allowed to enter the model at the 95% significance level. The crossvalidated skill is estimated as the correlation between observed and retrospective hindcast WEA_{isv} on the verification periods only, after having standardised the predictors and WEA_{isv} using the standard deviations of the training periods.

The three SST indices (defined in Fig. 11b) are never selected in the stepwise models, while the selected atmospheric indices may change according to the training periods. Nevertheless, such changes seldom occur for the models that use less than six predictors. Including more predictors does not really inflate the skill, but largely decreases the stability of the predictors selected. These linear stepwise models are discussed in Section 4, especially the one with five predictors, which helps us to decipher the different mechanisms involved in the intraseasonal variability of the low-cloud cover over WEA. Lastly, we performed the same crossvalidated stepwise models on low-pass and high-pass ISV variations.

3 | RESULTS

3.1 | Effect of intraseasonal variations on unfiltered LCF

As many preprocessing steps are used to extract ISV of the stratiform cloud cover, and also because ISV represents, at best, a moderate fraction of the whole variance, it is relevant to check the effect of intraseasonal variations seen through WEA_{isv} onto unfiltered stratiform cloud cover. To do this, we considered the five quintiles (q1–q5 from the lowest to the highest low-cloud cover) of WEA_{isv} and examined the associated modulations in daily ERA5 LCF, in the three-hourly unfiltered observed LCF (spatially averaged over the cloudiest sector, i.e., black dashed line in Figure 1a), and in the occurrence of the canonical three diurnal types defined in Moron et al. (2023), respectively representing overcast conditions all day long, afternoon clearings and clear days. As expected from the definition of WEA_{isv}, the largest signal is observed over the cloudiest sector, that is the coastal plain, windward slopes of the modest mountains (Massif du Chaillu, Mont Cristal, Plateaus Batéké, Figure 1a) as well as the hills and plateaus themselves (Figure 2a), while the differences amongst the quintiles are negligible further east toward the Congo Basin. The rather frequent afternoon clearings, or even clear days, over Gabon and SW RC in q1 of WEA_{isv} (Figure 2a,f) are also associated with less cloudy conditions off the coast and over the eastern equatorial Atlantic (Figure 2k). On the contrary, q5 of WEA_{isv} shows 75% or more of overcast days (Figure 2e), a +2 oktas anomaly peaking in the afternoon (Figure 2j) over the cloudiest sector and anomalously cloudy conditions off the coast (Figure 2o). These opposing anomalies are also observed for q2 (Figure 2b,g,l) and q4 (Figure 2d,i,n), but with an expected weaker amplitude. Logically, q3 (Figure 2c,h,m) corresponds to the climatological JJAS conditions. So, as observed at the interannual time-scales (Moron et al., 2023), the main ISV signal could be summarised mostly through the level of afternoon clearing over the cloudiest area of Gabon and SW RC.

3.2 | Vertical structure of atmospheric anomalies related to WEA_{isv} at local scale

We first explore the synchronous and lead/lagged (at the three-hour resolution) linear correlations between WEA_{isv} and the vertical thermodynamic structure of the atmosphere between 1000 and 200 hPa over Gabon (spatial average over 3° S–2° N, 10–14° E, Figure 3).

We interpret the correlations in Figures 3–9 from the atmospheric anomalies related to cloudier conditions than usual (i.e., a positive anomaly of WEA_{isv}). Indeed clearer conditions than usual are, by definition, related to opposite anomalies in T, q, u, v and w. Anomalously cloudy conditions at day 0 (D0 in Figure 3) are preceded by (i) warm anomalies from the surface to 450 hPa, peaking in the middle troposphere around 700 hPa (i.e., the free atmosphere above the cloud deck) around mid day −1; (ii) generalised low and middle tropospheric anomalous easterlies (mostly

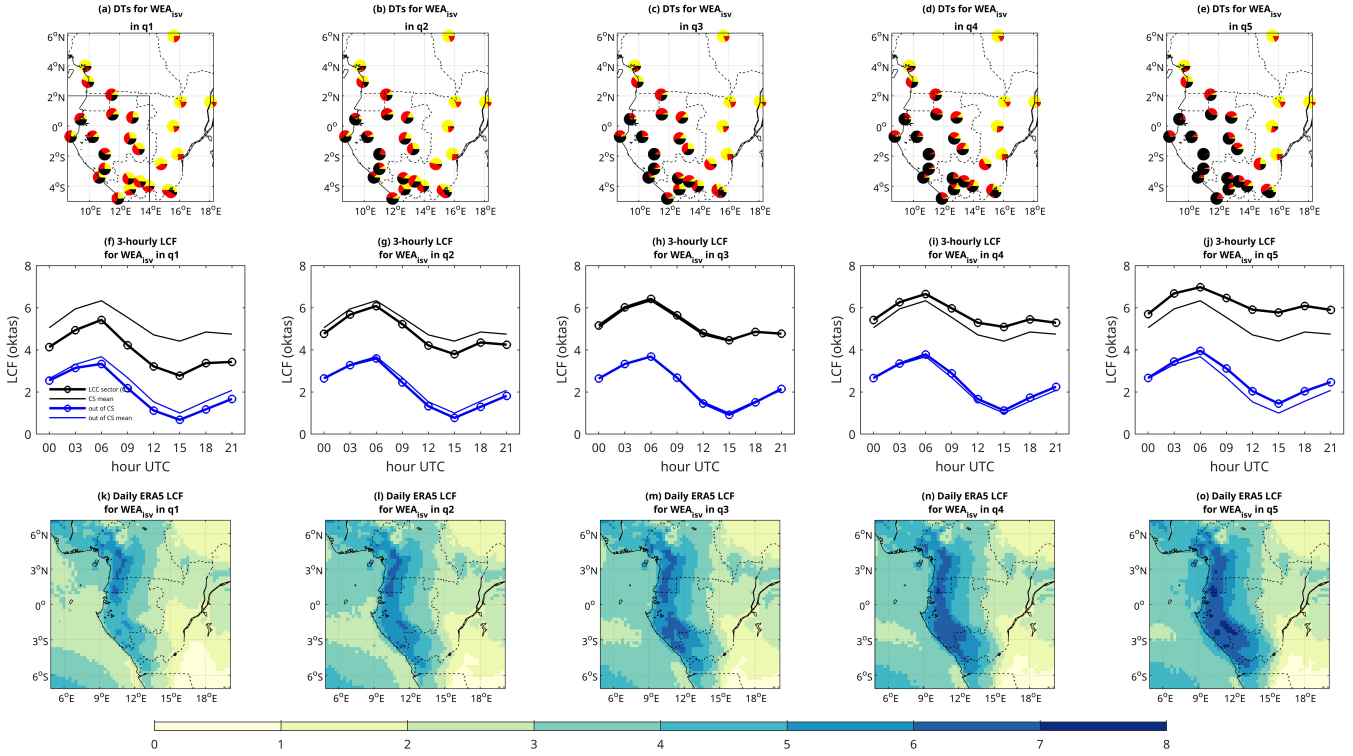

FIGURE 2 (a–e) Relative frequency of the three diurnal types (DTs) of LCF defined in Moron et al. (2023), depicting clear (yellow), clear afternoon (red) and overcast (black) days when WEA_{isv} is in its first (q1), second (q2), third (q3), fourth (q4) and fifth (q5) quintile. The black line in panel (a) contours the cloudiest sector. (f–j) Spatial average of raw three-hourly low-cloud fraction (LCF, in oktas) over the cloudiest sector (cf. Figure 2a) (black lines) and outside this area (blue lines) for q1–q5 of WEA_{isv}. The bold lines with circles represent the spatial averages for each quintile and the thin lines represent the climatological spatial averages. (k–o) Mean daily ERA5 LCF (in oktas) prefiltered using convective rainfall (see text) for q1–q5 of WEA_{isv}.

NE above 900 hPa and SE below 950 hPa, Figure 3); and (iii) anomalously moist air below 700 hPa, with a peak amplitude between 900 and 800 hPa (Figure 3), the usual top of the stratiform cloud deck (Champagne et al., 2023; Dommo et al., 2018). There is also an anomalous ascent between 900 and 800 hPa, while anomalous subsidence is seen above 800 hPa (Figure 3).

From late day −1 and early day 0, the low-level winds below the cloud deck veer clearly to anomalous SW (below 900 hPa) and NW (above 900 hPa), while the temperature anomalies switch to negative values, just after the low-level winds veer to westerlies (Figure 3). These cold anomalies from early day 0 are strongest during daytime, with a decreasing amplitude to day +2, while warm anomalies below 950 hPa and during late nights are still observed on day +1 and day +2 (Figure 3). These varying thermal anomalies across the diurnal cycle may be part of a local radiative response (stronger during the afternoon, Figure 3) to the increased stratiform cloud deck: a late-night anomalous warming, partly related to an increased greenhouse effect, and an anomalous cooling during most of the day, mostly driven by the reduced incoming solar radiation. This modulation of the diurnal cycle is superimposed on the cold anomalies below 800 hPa from day 0, linked to an intensified advection of cool Atlantic air by anomalous westerlies in low levels (Figure 3). A strong ascent is also seen just below the cloud deck during day 0 at night and morning, i.e., when the usual SW winds are the strongest (Dommo et al., 2022). The addition of westerly anomalies onto the SW basic flow denotes increased wind speed. This may enhance turbulence below and in the cloud deck (Champagne et al., 2023; Dommo et al., 2018), thus favouring the in-situ condensation of water vapour (Dommo et al., 2022), especially when it is combined with cold anomalies and antecedent anomalously moist conditions (as seen in Figure 3). Anomalous low-level ascent reverses to anomalous subsidence from the night between day 0 and day +1, with a decreasing amplitude (Figure 3), while a weak anomalous ascent is still observed during the anomalously warm late nights below 925 hPa (Figure 3). Again, these changes may be part of a local thermodynamic response to the low-level thermal anomalies due to the increased stratiform cloud deck.

In the middle troposphere, above the stratiform cloud deck, the T, q and wind anomalies just decrease in

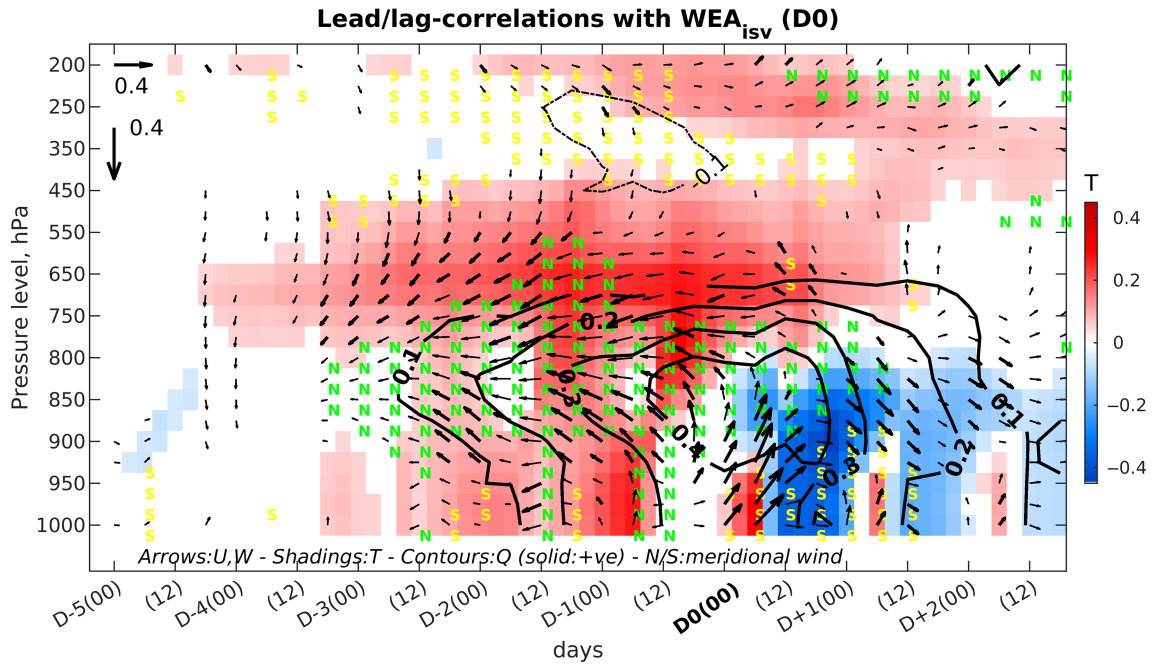

FIGURE 3 Lead–lag correlations (from day 5 to day +2 vs WEA$_{isv}$) between WEA$_{isv}$ and three-hourly ERA5 T, q, u, v and w spatially averaged over Gabon (3° S–2° N, 10–14° E). Shadings are for temperature. Arrows are for zonal and vertical winds. Letters are for meridional winds distinguishing only between negative (N) and positive (S) correlations. For clarity, wind information is shown at the six-hourly timescale. Full (dashed) black lines are for positive (negative) correlations of absolute humidity. Only significant correlations at the two-sided 95% level are shown.

amplitude, without any clear change in sign or direction on day 0, as observed below 800 hPa (Figure 3). Wind anomalies are the first to decrease, before the T and q ones. Lastly, note that warm anomalies are also observed above 300 hPa around day 0 (Figure 3).

3.3 | Atmospheric anomalies related to WEA$_{isv}$ at continental scale

Figures 4–6 show the lagged (from day −10 to day +3) correlations between WEA$_{isv}$ and T, q, u, v at 925 (Figure 4) and 700 hPa (Figure 5), and the geopotential height at 300 hPa (Figure 6). The lagged correlations have also been computed at 1000 (Figure S2) and 850 hPa (Figure S3) and the patterns are similar to those seen at 925 hPa (Figure 4), especially for the T and wind anomalies.

At 925 and 700 hPa, a first weak signal emerges at day −10 (Figures 4a and 5a) as an anomalous anticyclonic centre (referred to as 'H1' in Figure 4a–l) located over the central subtropical southern Atlantic. An anomalous cyclonic pattern (referred to as 'L1' in Figure 4c–h) shortly follows over southern Africa from day −8 (Figure 4c) to day 3 (Figure 4h). This pattern at 700 hPa (Figure 5) is located slightly west (by 5–15°) of the one at 925 hPa (Figure 4e). An anomalous anticyclonic curvature is also visible over the eastern coast of South Africa from day −7 (Figure 4d), and reinforces itself the following days. This suggests a slow or even a near-standing Rossby wave associating, for cloudier conditions over WEA, a reinforced St. Helena high and a trough centred over southern Africa, causing anomalous southerlies over the SE Atlantic, thus advecting anomalously cool air, and anomalous easterlies over the equatorial cold tongue (Figure 4e–j). The anomalous low pressure system 'L1', initially located over the SW and then over the central Republic of South Africa, is associated with anomalous northerly winds advecting anomalously warm air from the southern Congo Basin to tropical southern Africa from day −7 (Figure 4d–g). Overall, the H1–L1 dipolar pattern peaks from day −6 to day −3 (Figure 4e–h), then progressively decays. The 925-hPa zonal dipolar thermal pattern between southern Atlantic and southern Africa, visible from day −6 (Figure 4e–j), may indeed be intensified by the positive feedback from the static adjustment of pressure to the surface temperature anomaly. The signal in moisture at 925 hPa over the southern Atlantic is positive (i.e., cloudier conditions are associated with moister air), but relatively weak, since the increased wind speed over the ocean (increasing evaporation) may be partly offset by negative temperature anomalies due to advection (decreasing evaporation). The anomalous westerlies seen over western South Africa (Figure 4d–g) should also inhibit 'Berg' winds which advect dry warm air from the Namib and Kalahari deserts, adiabatically warmed

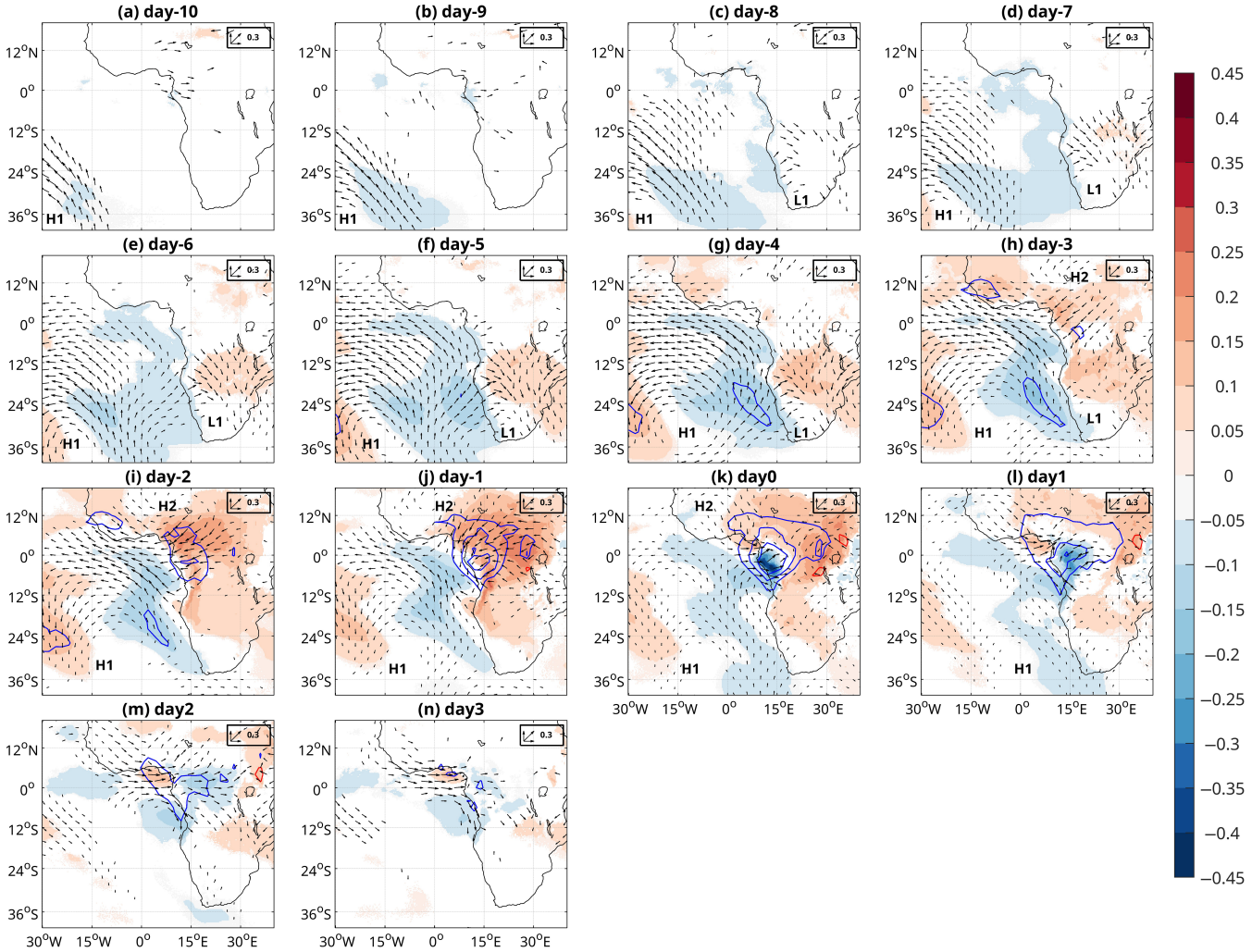

FIGURE 4 Lagged correlations between WEA_{isv} and daily T, u, v and q at 925 hPa from 10 days before to three days after the low-cloud variations over Western Equatorial Africa. The shadings show the correlations for temperature; vectors show the correlations for the wind with the scale for a value of 0.3 displayed in the upper right corner, and contours show those for the specific humidity. The shades and arrows are displayed only when the correlations (at least zonal or meridional component for the wind) are significant at the two-sided 99% level according to a random-phase test and contours are displayed every 0.1 value starting at 0.1 (blue) and −0.1 (red). For display purposes, the wind arrows are shown every 2° and specific humidity is linearly interpolated onto a 1° grid. 'H1', 'H2' and 'L1' are anomalous centres of action discussed in the text.

when flowing down the Great Escarpment towards the SE Atlantic. The low-level wind signal over tropical southern Africa almost disappears from day −3 (Figure 4h), while it is still visible over the southern Atlantic until day −1 at least (Figure 4j), reinforcing the hypothesis of a positive air–sea feedback near the surface able to sustain the low-level in-situ atmospheric anomalies (i.e., faster SE winds cool surface temperature, increasing the zonal geopotential and thermal gradients with the continent). However, the temporal association between these features does not necessarily establish that they are physically connected. This will be analysed in the next subsection.

With regards to signals north of and at the equator, a strong feature appears mostly from day −3 ('H2' in Figure 4h–k). Anomalous E–NE wind associated with warm anomalies are related to a westward moving anticyclonic pattern located East of Lake Chad. The E–NE anomaly intensifies on day −2 and day −1 while moisture over WEA tends to increase. It is not fully clear whether the wind anomaly is only related to the 'H2' pattern which is located over central Sahel on day −1 and vanishes thereafter (Figure 4j–n). The warm anomalies spreading from the Congo Basin to eastern Sahel from day −3 (Figure 4h) have also a larger spatial scale than the anomalous anticyclonic centre 'H2'. They coincide with more intense warm and easterly anomalies over WEA at 700 hPa (Figure 5h). Note that warm anomalies already exist on day −4 at 700 hPa over the equatorial Atlantic and WEA, still in association with anomalous easterlies (Figure 5f,g). In summary, the rather

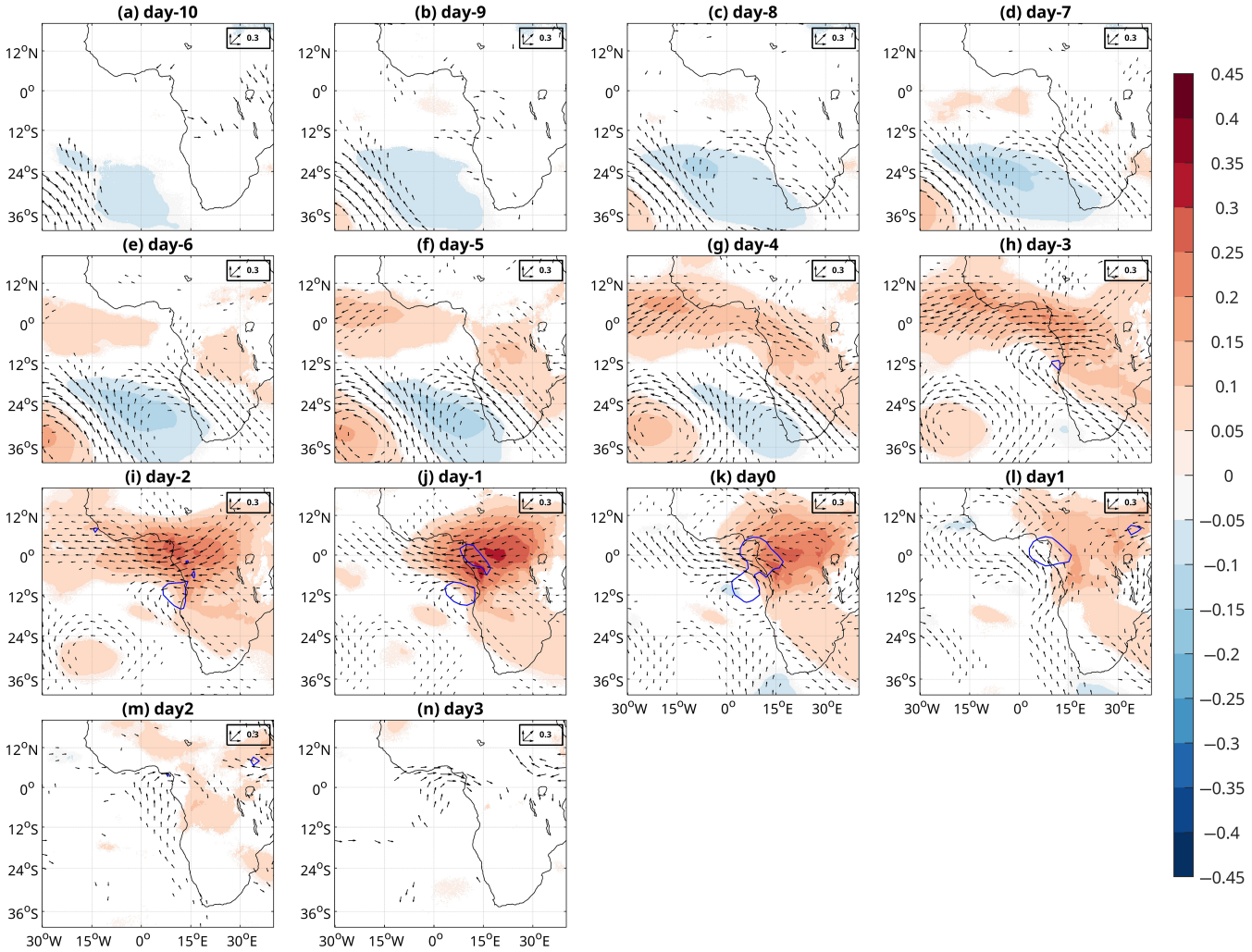

FIGURE 5 Same as Figure 4 except for 700 hPa T, u, v and q.

strong E–NE anomalies to the east of WEA, mostly from day −3 at 925 hPa and 700 hPa, advect anomalously warm and moist air over WEA, as already observed in Figure 3.

The low-level wind anomalies over WEA and the adjacent equatorial cold tongue clearly change from day −2 (Figure 4i) to day 0 (Figure 4k) while those observed at 700 hPa are near-constant (Figure 5i–k): on day 2, anomalous easterlies are recorded over the whole equatorial zone, decreasing to near zero just off the WEA coast on day −1 (Figure 4j), and switching to anomalous westerlies on day 0 (Figure 4k). Transient significant cold anomalies are then observed at 925 hPa (Figure 4k,l) and 1000 hPa (Figure S2k,l) and with a larger amplitude at 850 hPa (Figure S3k,l) over the cloudiest area of WEA, that is, windward of and over the mountains. This could be related either to advection of cold Atlantic air or to cloudier conditions reducing the incoming solar radiation during the day (but increasing the greenhouse effect during the night, Figure 3).

The signal observed first over the southern Atlantic, and shortly after over southern Africa, suggests a slow or even near-standing Rossby wave. This hypothesis is further explored by considering the correlations between WEA_{isv} and z at 300 hPa over a larger spatial window extending westward to South America (Figure 6). A clear dipolar pattern is indeed observed over the southern subtropics combining a positive pole around 30° W and a negative pole around 0° from day 9 (Figure 6b). The correlations peak in amplitude between day −6 and day −4 (Figure 6e–g). Note also the emergence of a positive correlation near the equator mostly from day −6 (Figure 6e). Two separate lobes of significant positive correlations, one off the Brazilian Nordeste and the other over equatorial eastern Africa (Figure 6e–g) merge at day −3 (Figure 6h). The positive correlations near the equator then strengthen till day −1 (Figures 3 and 6j), while the E–W dipolar pattern over the southern Atlantic has almost vanished.

Analysing the correlations on 10-day filtered data brings subtle nuances to these findings. First, the pattern

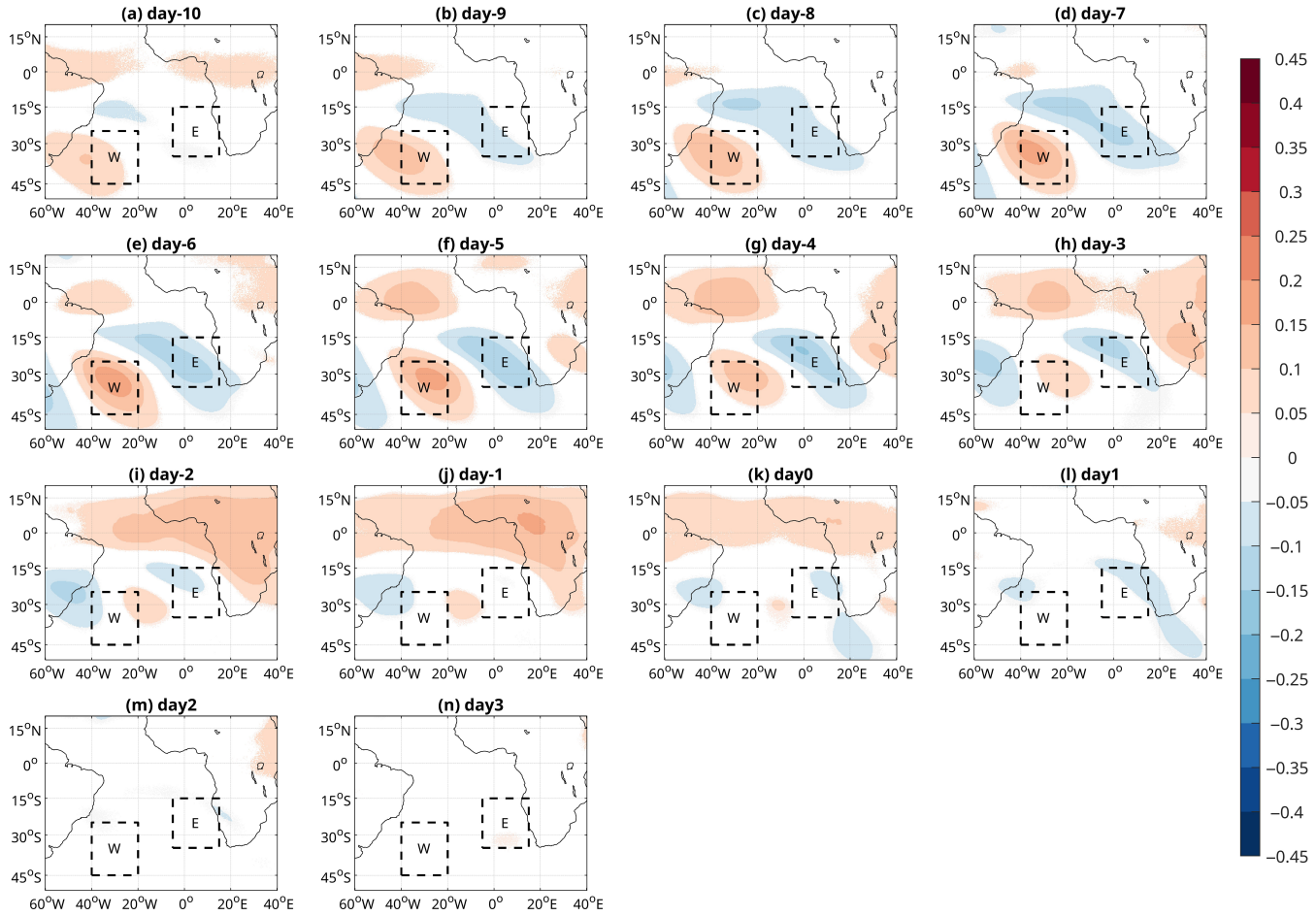

FIGURE 6 Lagged correlations between WEA_{isv} and daily geopotential height at 300 hPa from 10 days before to three days after the low-cloud variations over Western Equatorial Africa. The shadings show the significant correlations at the two-sided 99% level according to a random-phase test. The dashed boxes identify two sectors used to describe the amplitude of a Rossby wave between the western (W) and eastern (E) box.

emanating from the subtropical South Atlantic seems mostly restricted to low-pass ISV (Figures S4 for 925 hPa and S6 for 700 hPa) as it persists from day −6 (Figures S4e and S6e) till day +3 (Figures S4n and S6n), and it is absent in correlations with the high-pass-filtered data (Figure S5 at 925 hPa). Note also that the signal at 700 hPa, combining anomalous warming and easterlies, is stronger and again more persistent for low-pass-filtered variations (Figure S6) than for unfiltered ones (Figure 5). For the high-pass-filtered data (Figures S5 at 925 hPa and S7 at 700 hPa) the most significant correlations are restricted to the subequatorial area roughly between 10° S and 10° N. There is now a clear switch at 700 hPa (also seen at 925 hPa with a weaker amplitude), with transient westerly and cold anomalies on day −5 and day −4 (Figure S7f,g) veering to anomalous easterly and warm anomalies on day −2 and day −1. Curiously, these easterlies and warm anomalies are also seen at day +1 (Figure S7l), while they are weak over WEA on day 0 at 700 hPa (Figure S6k), and local westerlies and cold anomalies are observed at 925 hPa (Figure S5k). It is also interesting to note that correlation patterns at low pass and high pass may be opposite, thus explaining the weak correlations using unfiltered data. Such opposite relationship occurs for example over the equatorial Atlantic at 925 hPa on day −6 and day −5, where anomalous westerlies (respectively easterlies) are observed for high-pass- (respectively low-pass)-filtered data (Figures S5e,f and S6e,f).

In order to better understand the mechanisms explaining WEA_{isv} the lagged teleconnections with two different areas, namely the subtropical southern Atlantic and the subequatorial area, are next explored.

3.4 | The pathway from the South Atlantic

Figure 7 shows the lagged correlations of z at 300 and 925 hPa (Figure 7a,d,g,j), T, u, v and q at 700 hPa (Figure 7b,e,h,k) and 925 hPa (Figure 7c,f,i,l) with a

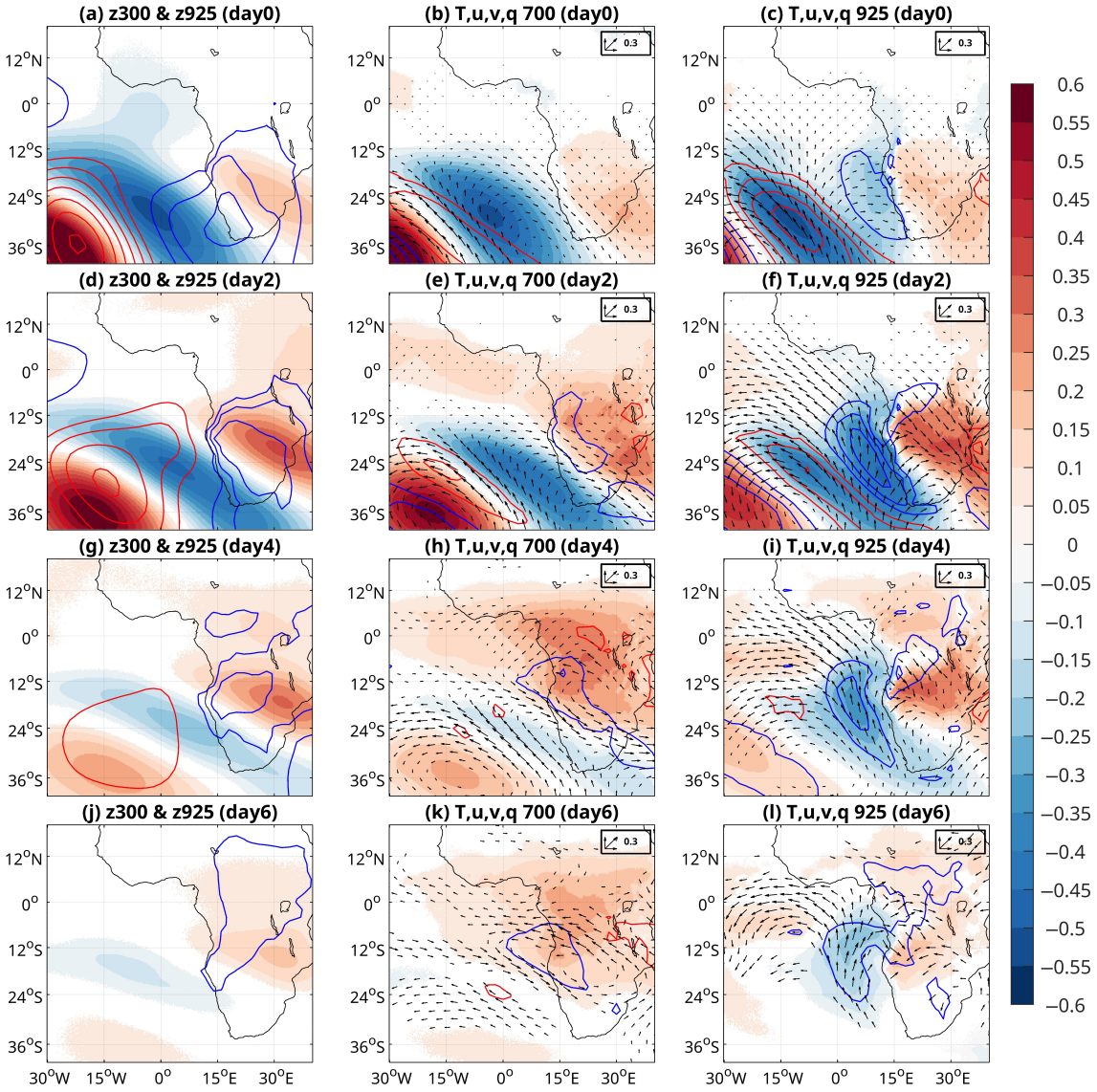

FIGURE 7 Same as Figure 4 except that the lagged correlations are computed between the 300-hPa geopotential index (dZ300, see Figure 6) of (40–20° W, 45–25° S) minus (5° W–15° E, 15–35° S) starting for lags of no, two, four and six days after dZ300 for (left column); z at 300 hPa (shadings) and at 925 hPa (contours with red for values from 0.1 with an interval of 0.1 and blue for values from −0.1 with an interval of 0.1); (middle column); u, v, T, and q at 700 hPa (same displays as in Figures 6 and 7); (right column): u, v, T, and q at 925 hPa (same displays as in Figures 6 and 7).

dipolar index (dZ300) measuring the difference in 300 hPa geopotential between the central (40–20° W, 45–25° S) and eastern (5° W–15° E, 15–35° S) southern Atlantic (Figure 6). Our interpretation follows the sequence associated with a positive anomaly of dZ300, that is an upper anticyclonic ridge over the western-central South Atlantic combined with an upper cyclonic trough above SE Atlantic. The zero lag correlations show a clear expected dipolar, slightly tilted, structure at all levels considered (Figure 7a–c), combining, at 925 hPa, a strengthened St. Helena high-pressure system with a downstream anomalous low, standing over South Africa at day +2 (Figure 7d,f), while the signals north of 10° S are still weak (Figure 7a–c). The cooling/moistening at 925 hPa over the Benguela area is associated with anomalous westerlies on day 0 (Figure 7c), then anomalous southerlies from day +2 (Figure 7f). The increased thermal land–sea contrast at 925 hPa from day 0 to day +6 is able to sustain partly the increased southerlies along SW Africa, due to the anomalous increased (decreased) surface pressure over the anomalously cold (warm) SE Atlantic (southern Africa). Anomalous SE–E winds strengthen also over the equatorial cold tongue on day +2, before progressively decaying (Figure 7f,i,l). The correlation between dZ300 and the SST over the equatorial cold tongue peaks at day +8 ($r = -0.18$), while the one with the SST over the Benguela current

peaks just before, at day +7 ($r = -0.16$), consistent with a northward-propagating signal originating from the southern Atlantic. Except for the slight tilt, the signals at 700 hPa match those observed at 925 hPa even if the thermal signals above the Benguela current are stronger near the surface, reinforcing the hypothesis of a positive feedback in the shallow marine boundary layer.

The anomalies south of 10° S tend to weaken after day +2 (Figure 7g–l), while significant anomalous SW–W winds appear over WEA at 925 hPa from day +4 (Figure 7i) and then propagate eastward, covering most of the Congo Basin from day +6 (Figure 7l). Note also the persistent anomalous warming over equatorial Africa, appearing on day +2 at 700 hPa (Figure 7e) and day +4 at 925 hPa (Figure 7i). This warming is stronger at 700 than at 925 hPa, and persists till day +6 (Figure 7k,l) while anomalies at 300 hPa over the southern Atlantic are very weak at this lag (Figure 7j).

It is interesting to note that the spatial pattern of correlations with dZ300 at zero lag (Figure 7a–c) almost perfectly matches the one with WEA_{isv} on day −8 (Figures 4c,5c and 6c) especially south of 10° S (pattern correlations between the same variables are usually >0.6 for the spatial window of Figures 4–5 and usually >0.75 south of 10° S). So, overall, the statistical teleconnection involving dZ300 (Figure 7) includes most of the signals related to WEA_{isv} (Figures 4–6). The correlations between dZ300 and WEA_{isv} peak to 0.17 when dZ300 leads WEA_{isv} by six days, reinforcing the hypothesis of a causal link initiated by the Rossby wave over the South Atlantic. The favourable ingredients to cloudier than usual conditions over WEA (Figures 4, 5) and possibly initiated by the dZ300 positive anomaly (Figure 7) include: (1) the overall strengthening of the St. Helena high; (2) a cooling of the eastern South Atlantic and then, the equatorial cold tongue; (3) anomalous low-level westerlies advecting cool maritime air toward WEA, (4) warm anomalies at 700 hPa over WEA and the whole Congo Basin, and associated with anomalous easterlies. At least two ingredients propitious to more clouds over WEA (Figures 4–5) do not really appear on the sequence linked to dZ300 (Figure 7); it is (i) the strong positive in-situ anomaly of moisture at low levels (and peaking near 850 hPa, which corresponds to the top of the stratiform cloud deck) on day 0 (Figure 4k), and (ii) the anomalous northeasterlies associated with anomalous warm air NE of WEA from day −3 at 925 hPa (Figure 4h–k).

The main difference between correlation patterns with low-pass- and high-pass-filtered data (not shown) is found mostly in the amplitude of the warm anomalies at 700 hPa over equatorial Africa: it is strongly reduced for the high-pass-filtered data. The tilted and alternate pattern over subtropical southern Atlantic is observed for both cases (low pass and high pass), but with a larger amplitude for the former (not shown).

3.5 | The regional pathways

To depict and understand the teleconnections not clearly related to dZ300, we choose two atmospheric indices spatially averaged over WEA (10° E–15° E, 5° S–5° N) from day −5 to day +5: (q850_WEA), (Figure 8a–k) and u925_WEA (Figure 9a–k). q850_WEA is the index which is the most correlated to WEA_{isv} at zero lag ($r = 0.49$, Figure 3) and this correlation shows a 'slow' variation, that is a positive correlation emerging a few days before WEA_{isv} (Figure 8a–f) and gradually decreasing after day 0 (Figure 8g–k). Note that considering 925 or 1000 hPa instead of 850 hPa for the specific humidity leads to very similar, albeit slightly weaker, correlations with WEA_{isv}. The latter is close to the usual top of the low cloud (Champagne et al., 2023), and any change occurring here may be critical for the variations of the low-cloud cover.

u925_WEA is less correlated to WEA_{isv} ($r = 0.19$ at zero lag) but, contrary to WEA_Q850, it shows a clear switch between negative correlations, peaking at $r = -0.19$, at day −2, and positive correlations from day 0. More interesting, u925_WEA and q850_WEA are negatively correlated at zero lag (−0.32) and the correlation peaks even to −0.52 when u925_WEA leads q850_WEA by one day. In other words, both indices contribute positively to WEA_{isv} (i.e., more low-level clouds are related to a combination of in-situ anomalous westerlies strengthening the basic flow, shortly after anomalous easterlies at 925 hPa, and a high moisture content at 850 hPa), but anomalous westerlies at 925 hPa are more or less synchronous (and shortly lead) to a negative moisture anomaly at 850 hPa. The negative correlation at zero lag between u925_WEA and q850_WEA is fully consistent with the fact that the Atlantic airmass holds less moisture than the continental Africa one primarily due to its lower temperature (Moron et al., 2023). The continental air mass staying north and east of WEA is warm and moist since during the boreal summer it originates from the Congo Basin where rainfall still occurs and forests provide moisture to the atmosphere. Both the u925_WEA and q850_WEA indices thus reveal different mechanisms contributing partly to WEA_{isv}. Figures 8 and 9 explore the relationships between these two indices and T, u, v and q at the corresponding level from day −5 to day +5.

The lead–lag correlations with q850_WEA show two distinct features. First, a weak increase of the western-central part of St. Helena high is visible on day −5 (Figure 8a) to day −3 (Figure 8c). This reflects a weak relationship with dZ300 ($r = 0.14$ when dZ300 leads

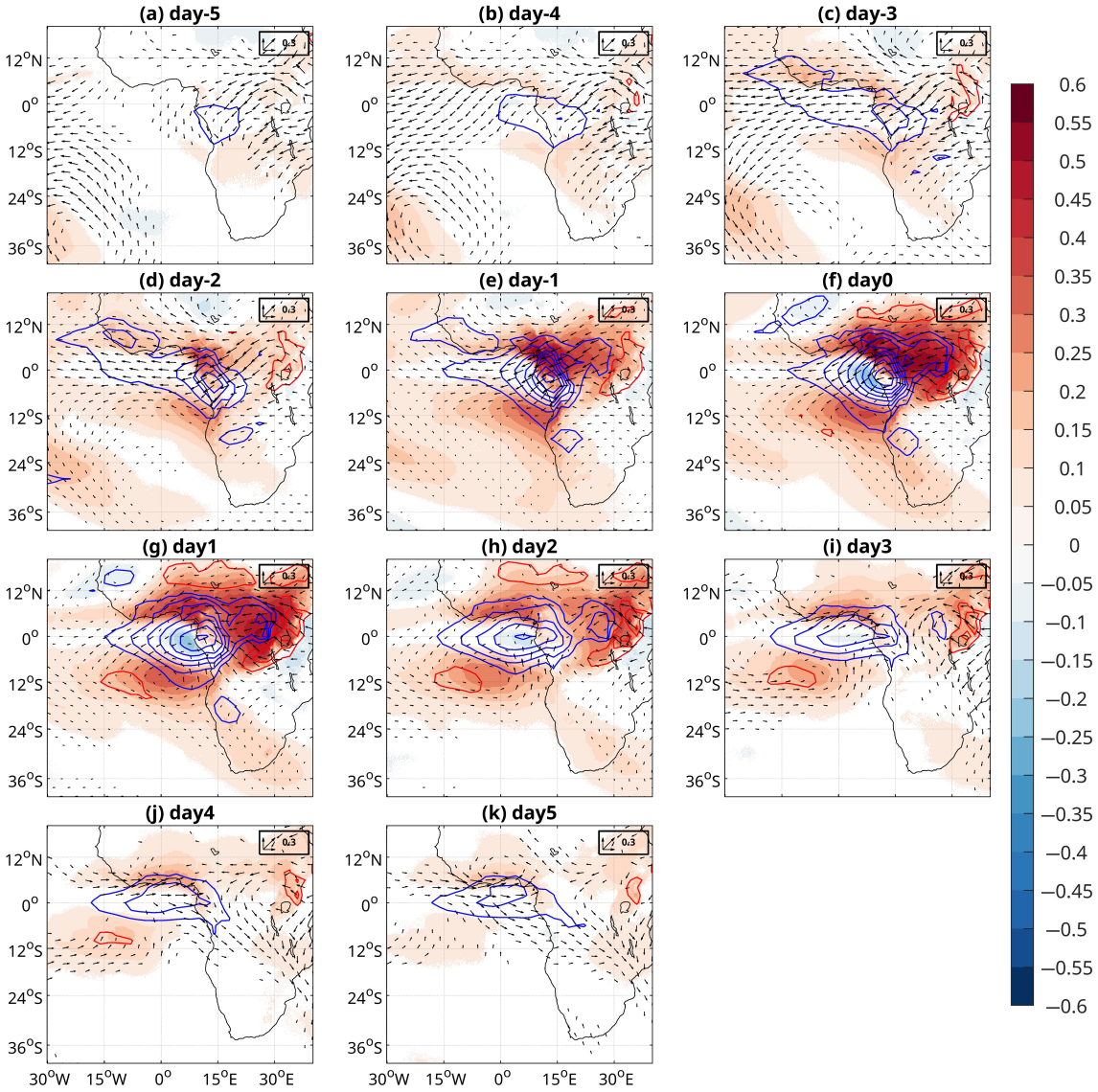

FIGURE 8 Lagged correlations at 850 hPa from five days before to five days (days are computed as the average of three-hourly records) after q850_WEA for the intraseasonal variability. The shadings show the correlations for temperature; vectors show the correlations for the wind with the scale for a value of 0.3 displayed in the upper right corner, and contours show those for the specific humidity. The shades and arrows are displayed only when the correlations (at least zonal or meridional component for the wind) are significant at the two-sided 99% level according to a random-phase test and contours are displayed every 0.1 value starting at 0.1 (blue) and −0.1 (red). For display purposes, the wind arrows are shown every 2° and specific humidity is linearly interpolated onto a 1° grid.

q850_WEA by five days). Second, an E–NE anomaly associated with a warm anomaly is visible over the Congo Basin and Sudanian belt from day −5 (Figure 8a), that strengthens and extends westward on the following days. Again, an anomalous anticyclonic cell over the eastern Sahel is clearly visible on day −3 (Figure 8c) that then shifts westward and decreases in intensity. We cannot state that the E–NE anomaly is entirely driven by this anticyclonic cell which is compatible with a ridge behind an easterly wave (Berger, et al. 2025; Gu et al., 2004; Thorncroft & Hoskins, 1994), but both phenomena seem coincident in time. The continental warm anomaly intensifies from day −2 (Figure 8d) with two lobes surrounding the positive moisture anomaly over WEA. The warm anomaly is stronger and larger from the Guinea Gulf to the Congo Basin on day 0 and day +1 while a small weak cold anomaly appears at zero lag just off WEA (Figure 8f,g). The easterly anomaly over equatorial and Sudanian Africa weakens clearly from day +1 (Figure 8g) and anomalous westerlies are observed over the equatorial cold tongue from day +3 (Figure 8i), while the positive moisture anomaly decreases.

With regards to u925_WEA (Figure 9a–k), the first consistent signal is a large-scale warming of the whole

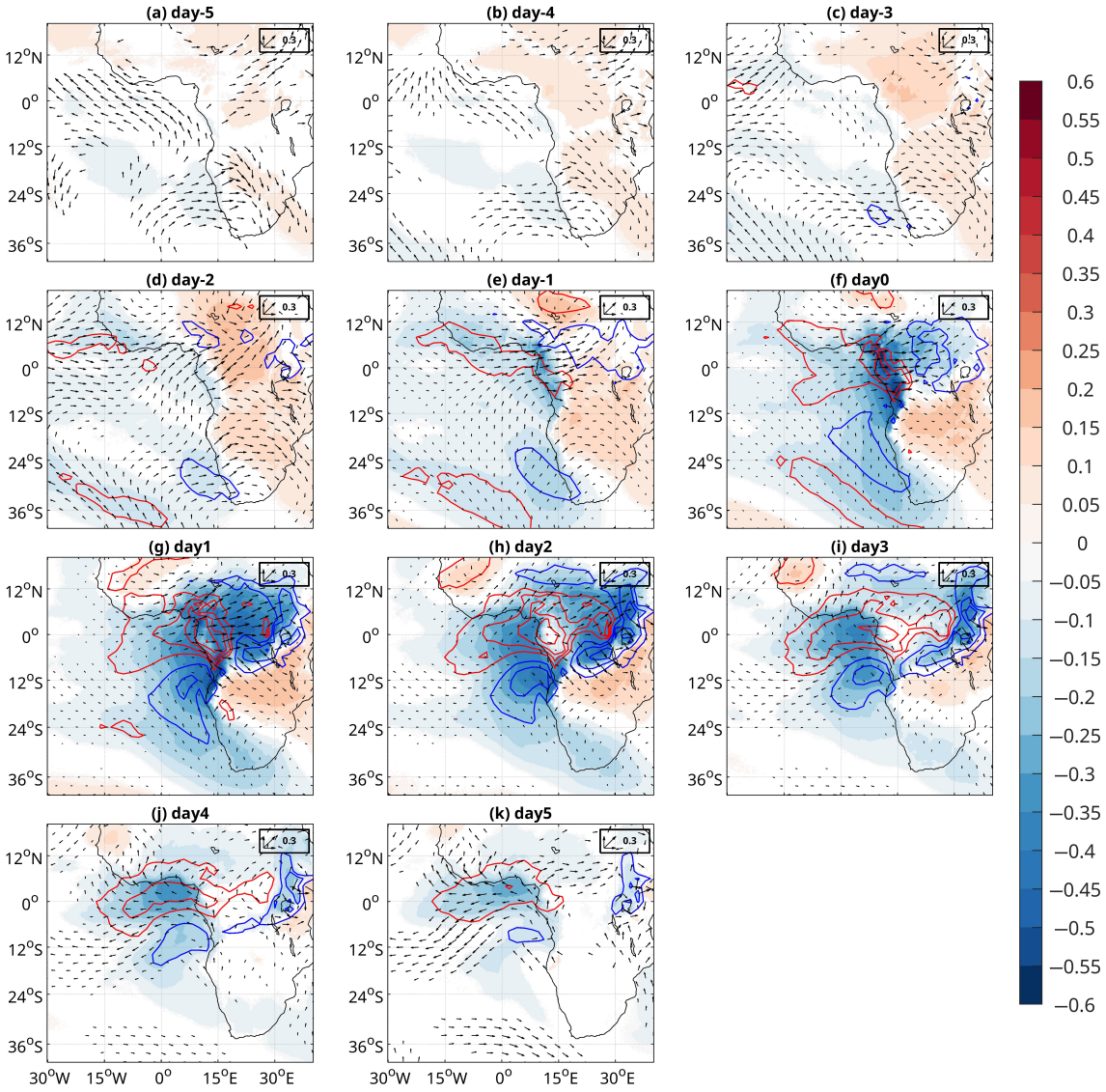

FIGURE 9 Same as Figure 8 except that the target is u925_WEA and the T, u, v, q fields are at 925 hPa.

African land mass as soon as day −4 (Figure 9b) which peaks NE of WEA on day −2 (Figure 9d). The warm anomalies are followed by W–SW anomalies over WEA from day −2 (Figure 9d), which strengthen the following days in combination with cold and dry anomalies peaking over WEA at zero lag (Figure 9f). It is clear that the wind anomaly leads the temperature anomaly over and downstream WEA from day −2: preceding warm anomalies over the Congo Basin are replaced by cold anomalies moving eastward, shortly (~1 day) following the westerly anomaly (Figure 9d–h). The westerly anomaly gradually vanishes first on the equatorial cold tongue from day +2 (Figure 9h) and an easterly anomaly appears here two days later (Figure 9j,k).

In summary, q850_WEA and u925_WEA reveal partly different and opposing processes; the increasing moisture content at 850 hPa over WEA is clearly induced by a E–NE anomaly advecting moisture from the north of the Congo Basin or eastern Sudanian belt, partly coincident with, if not driven by, a westward easterly wave whose amplitude is the strongest over the eastern Sahel. The increased low-level moisture content till the top of the cloud deck has a positive effect on the thickening of the cloud deck which may then be harder to break up. u925_WEA shows partly contradictory signals since increased westerlies advect anomalously cold, but also anomalously dry Atlantic air over WEA. The cold anomalies at low levels increase the static stability and decrease the threshold to condensate the water vapour, even if the Atlantic airmass is drier than its Congo Basin counterpart. Schuster et al. (2013) also noted that during the West Africa monsoon season, low-level cloud formation is associated with dry air advection from the Gulf of Guinea, but this is counteracted by cold air advection and boundary

layer turbulence. When considering separately low- and high-pass variations, correlations with q850_WEA are larger at least for the temperature and humidity for the former ones, and the wind signals are broadly persistent with anomalous easterlies over the equatorial zone.

u925_WEA shows a switch of the zonal wind over the cold-tongue area (see also Figure 3) while q850_WEA is preceded by an E–NE anomaly starting over the continent and peaking at day −1/day 0, and is followed by anomalous westerlies at day +3 and day +4. Neither index shows large negative autocorrelations at day 3–6 (minimum autocorrelation is −0.03 at day 6 for u925_WEA and −0.004 at day 10 for q850_WEA) but q850_WEA is more persistent than u925_WEA (autocorrelation at day 2 is 0.21 for u925_WEA and 0.44 for q850_WEA). It suggests that the switching between easterlies and westerlies over the cold-tongue area and WEA may be either intermittently self-sustained or driven intermittently by an external process (see section 3.6) rather than induced by a systematic internal quasi-periodic oscillation.

3.6 | Potential influence of convectively coupled equatorial waves (CCEWs)

We first evaluate the impact of 6 CCEWs on WEA_{isv} through an analysis of variance, that is, the contribution of total variance due to the four (or eight in case of ER and MJO) phases. We also estimate the fraction of variance due to strong phases defined as the normalised amplitude in each wave phase (Schlueter et al., 2019a). The percentage of explained variance of WEA_{isv} is negligible (0.3% at maximum) for MRG, EIG, TD and ER, even when only the strong phases are considereded. MJO accounts for 0.52% (1.28%) of the variance of WEA_{isv} when all intensities (only strong phases) are considered. The KW-related variance of WEA_{isv} is around three times the one of MJO with 1.7% (3.9%, only strong phases). This amount of explained variance is still very modest but the anomaly pattern related to KW (Figure 10) is interesting.

Figures 10 and S10 indicate that strong KW have the highest impact on T and u fields over the central Congo Basin. The eastward-travelling wave takes the form, in the lowest levels, of a signal almost symmetric to the equator which combines anomalous westerlies (easterlies) with lower (higher) land temperature than usual. The belt of anomalous easterlies (and warm anomalies over land) moves from the Gulf of Guinea area in phase #4 (Figure 10d,h,l), to WEA in phase #1 (Figure 10a,e,i), the central Congo Basin in phase #2 (Figure 10b,d,j) and eastern Africa in phase #3 (Figure 10c,g,k). Over the equatorial Atlantic and WEA, the anomalous easterlies in phases #4 and #1 are replaced by anomalous westerlies in phases #2 and #3. When all KW phases are considered, the mean lag to switch from a given phase to the next one, excluding the self-transition (when the same phase persists from one day to the next), equals 5.1 days. Considering only the strong KW phases increases the mean lag to 10.6 days. The mean WEA_{isv} anomaly peaks for phase #2 (0.18 in standardised units) and phase #4 (−0.17) when all KW intensities are considered (and 0.23 and −0.28, respectively, when only the strong phases are considered). These anomalies are modest in amplitude but KW could trigger a sequence of cloudy days in WEA. In particular, Figure 10e,i shows that the anomalous easterlies convey warm and moist air from the continent to WEA in phase #1, just before the WEA_{isv} peak (phase #2, 1–2 days later). At this time, the low-level moisture convergence between the anomalous westerlies and easterlies accounts for the persistence of the positive moisture anomaly (Figure 10f,j), while the temperature starts to decrease due to the advection of the Atlantic airmass which increases turbulence in the planetary boundary layer.

4 | DISCUSSION

The mechanisms detailed in the previous section are synthesised using a crossvalidated stepwise linear regression model (Section 2.5) to select a set of key atmospheric indices involved in the ISV of the stratiform cloud cover over WEA (Figures 4–10). The full set of 120 atmospheric indices depict T, u, v, w, q at 1000, 925, 850 and 700 hPa over the six regional boxes WEA, SCONG, CONG, CT, NEQ, and BEN shown in Figure 11a. We also considered four additional atmospheric indices, that is, the dZ300 index corresponding to the Rossby wave patterns, z925 over the 'SH' (St. Helena) box, LTS over the 'WEA' box and OLR over the 'CONG' box to include variations of deep convection over the Congo Basin, which is reduced in JJAS, but not absent (Hart et al., 2019). Each index is named as ['variable,' 'level'_'AREA']. For example, t700_CONG is the spatial average of temperature at 700 hPa over the CONG box. Note that three SST indexes (Figure 11b) were also computed over the 'CT' (Cold Tongue) area, a narrow coastal band (roughly 2° off the coast) off Gabon and SW RC ('GAB'), and over the Benguela area ('BEN'). The crossvalidated stepwise linear regression model selects the most significant predictors of WEA_{isv} (from a lag of −10 days to day 0) amongst these 127 indices. The crossvalidated skill is modest for lags larger than three days (Figure 12a). A model using only three variables performs almost as well as a model including more variables, but as the number of predictors increases the model becomes more unstable (Figure 12b). We show the indices the most frequently selected across

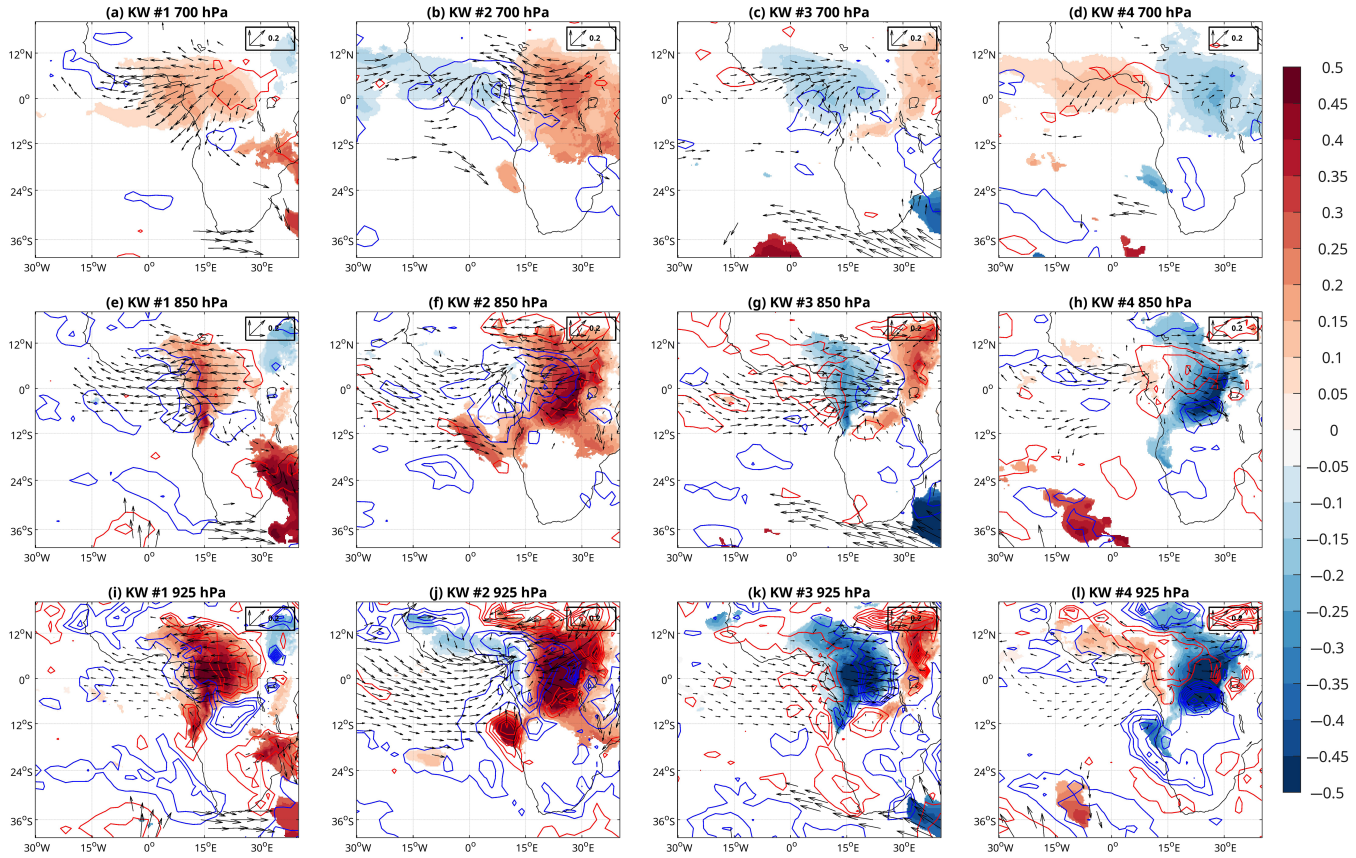

FIGURE 10 Mean intraseasonal anomalies of T (shadings in K), u, v (arrows in m/s) and specific humidity at 925, 850 and 700 hPa related to strong Kelvin waves. The T, u and v anomalies are displayed only when they are significantly different from 0 according to a Monte Carlo resampling made 500 times (JJAS sequences of Kelvin waves are randomly reshuffled). Positive (blue contours) and negative (red contours) values of specific humidity are shown from 5×10^{-5} with a contour interval of 5×10^{-5}.

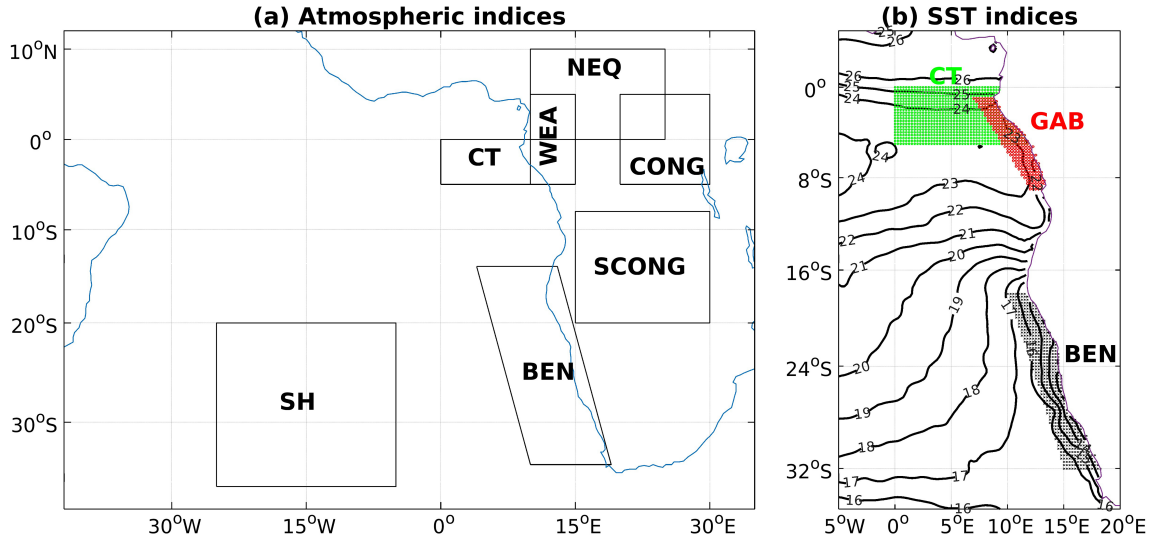

FIGURE 11 Location of the (a) atmospheric and (b) SST indices superimposed on the mean SST (°C) in JJAS 1971–2019.

the crossvalidated periods for a five-variable model, that is, the most explicative of both WEA_{isv} and of the regional oceano-atmospheric ISV. Note that we also present in Figure 12c–p some atmospheric indices, such as CONG_OLR or NEQ_u850, which are less robust predictors of WEA_{isv}, but serve as mediators in the conceptual

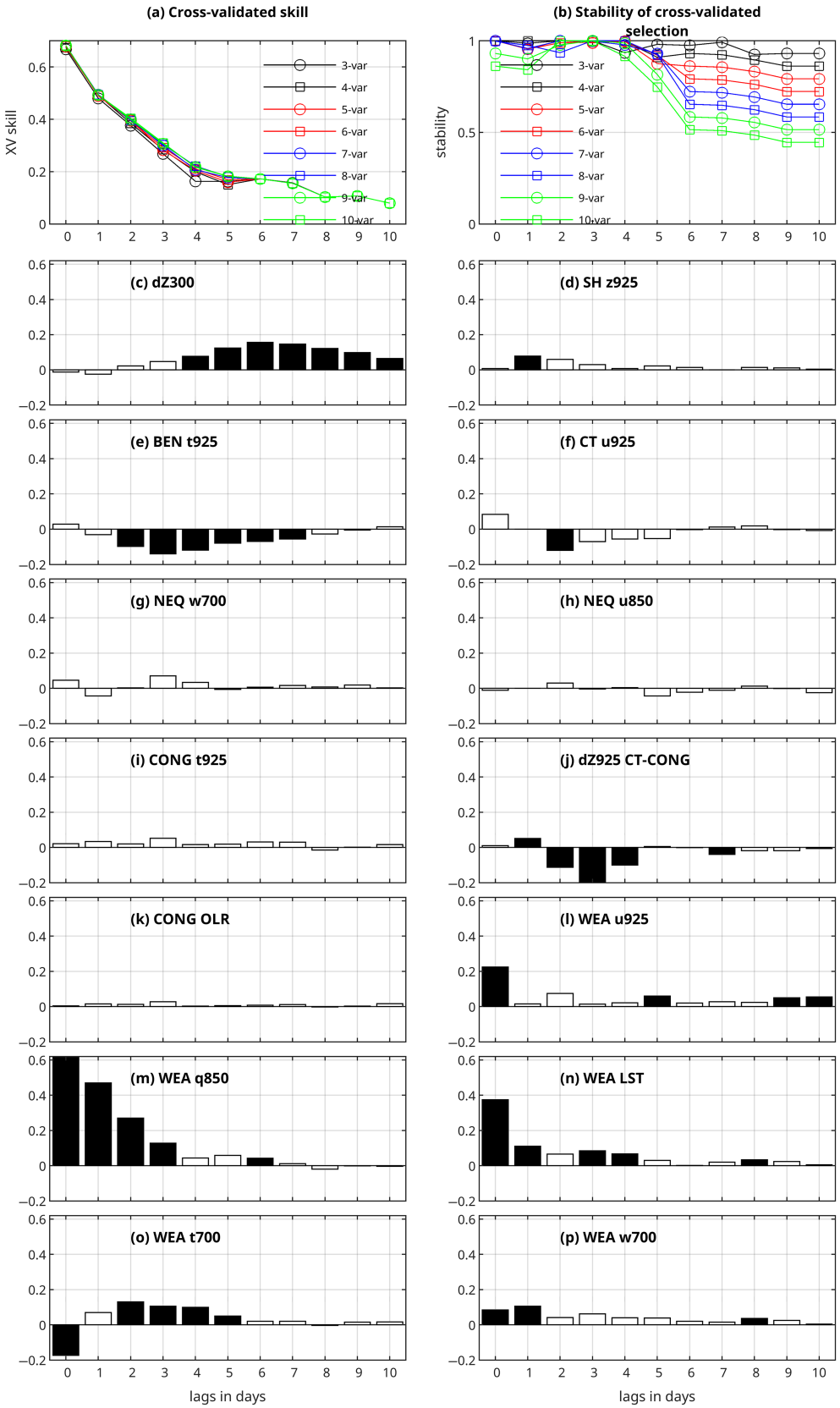

FIGURE 12 Crossvalidated stepwise linear model to estimate WEA_{isv} from atmospheric indices from lag −10 (atmospheric indices lead) to lag 0. The crossvalidation is done with one JJAS season withheld at each turn. (a) Crossvalidated skill (vs lags) of the stepwise model on the verification period using only 3–10 atmospheric indices. The number of variables is a maximum since there are not always more than 5–7 variables entering the model at the 95% significance level. (b) Stability of the atmospheric indices (vs lags) entering the stepwise model during the 49 training periods (a stability of 1 means that the same set of atmospheric indices is chosen across all the crossvalidation iterations). (c–p) Mean value of the parameter (vs lags) of each atmospheric index used in the stepwise model with five predictors at maximum. The black bars indicate that the parameter is significantly different from 0 at the two-sided 95% level during at least 25 training periods.

model we established (Figures 13 and 14). As the atmospheric indices are standardised to zero mean and unit variance, their amplitude scales their relative impact on WEA_{isv}.

As expected, the most important predictor is WEA_q850 at lag 0 (Figure 12m). It is also clear that the first explanatory atmospheric index is dZ300 with a significant impact from lag −10 and peaking on lag −6 (Figure 12c).

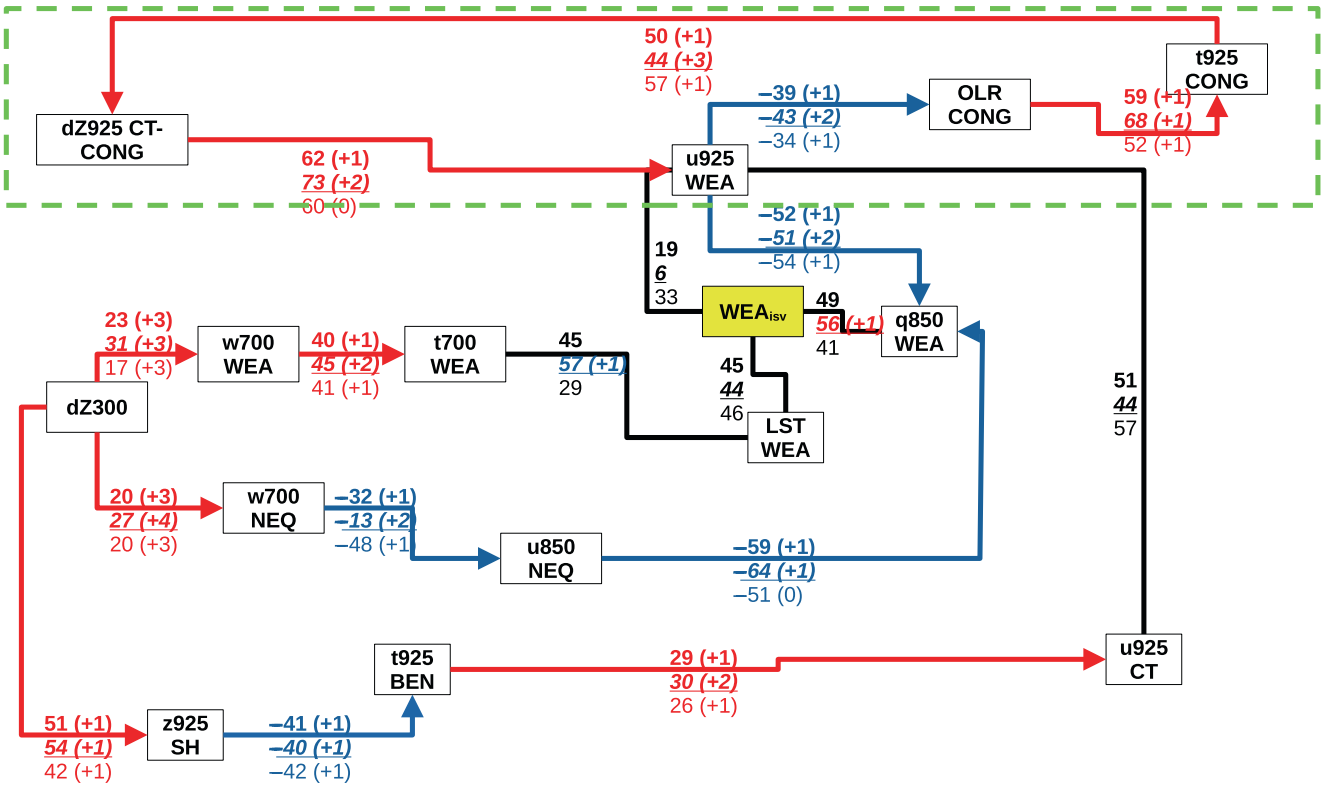

FIGURE 13 Lagged correlations (upper value in bold font is for unfiltered ISV; middle value in bold and italicised font is for low-pass (≥10 days) ISV variance and lower value in normal font is for high-pass (<10 days) ISV variance) between atmospheric indices defined in Figure 11b. The maximum absolute correlation multiplied by 100 (between day −10 and day +10) is indicated with the corresponding lag (in days) counted from the starting box of each arrow with positive correlation in red font and negative correlation in blue font. When the correlation peaks at zero lag, it is indicated as a black link without any arrow. The green box identifies a potential sustained mode of variation around WEA.

The atmospheric indices that follow, from lag −6 to lag −2, are BEN-t925, dz925, WEA_t700 and CT_u925 (Figure 12e,f,j,o). The local atmospheric indices WEA_u925, WEA_LST and mostly WEA_q850 (Figure 12l–n) usually increase their explanatory power till lag 0 with a constant polarity from lag −10. As expected, the explanatory power of the model applied on low-pass-filtered data (Figure S8) is slightly larger than the one on the high-pass-filtered data (Figure S9). The sequential order is modified for high-pass variations while dZ300 and BEN_t925 do not appear anymore as significant predictors of WEA_{isv} (Figure S9c,e). There are also clear switches in most of the other predictors sometimes just before lag 0 as for WEA_LST (Figure S9n).

Figure 13, based on a reduced set of lagged correlations, synthesises the different mechanisms involved in the ISV of the stratiform cloud cover over WEA (Figure 14). Remember first that the highest correlation at zero lag for WEA_{isv} is with q850_WEA ($r = 0.49$, Figure 3). This strong positive relationship contrasts with previous findings for the SE Atlantic sector. Over coastal Namib, Andersen et al. (2020) found that an anomalously dry free troposphere leads to more low clouds, through a stronger long-wave cooling of the boundary layer. Adebiyi and Zuidema (2018) found a similar association between increases in the mid-tropospheric moisture and decreases in low-cloud cover over the SE Atlantic Ocean. This points to the different nature of the low clouds over WEA as compared to those of the SE Atlantic and Namibian coast. They extend far to the interior, in a context where (i) the basic low-level flow (W–SW in JJAS, Moron et al., 2023) interacts with the topography through an efficient vertical mixing when winds are faster than usual (Dommo et al., 2022) and (ii) the excess moisture is advected from either the ITCZ area or the Congo Basin (rather than the Atlantic Ocean), by the mean easterly flow from and above 850 hPa (Moron et al., 2023). Dyer et al. (2017) demonstrated indeed that the dominant moisture sources over the Congo Basin are local evaporation and the Indian Ocean, while the Atlantic Ocean is a relatively small source. Fuchs et al. (2018) also established that, over the SE Atlantic Ocean (10–20° S, 0–10° E), drivers and processes (other than moisture) determining the stratocumulus cloud cover, vary spatially. For instance, while in

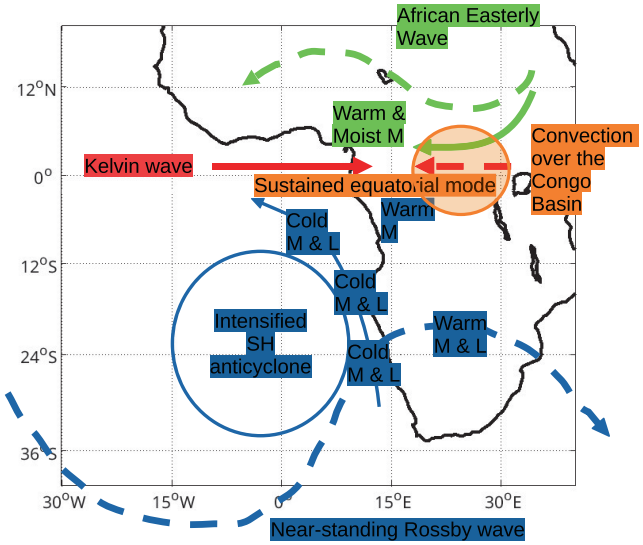

FIGURE 14 Synthesis of the drivers involved in the ISV variations of WEA_{isv}. The anomalies indicated in this figure lead to cloudier conditions than usual over WEA.

the southwestern subregion (i.e., Central SE Atlantic), the low-cloud fraction is sensitive to variations in LTS, in the northeastern subregion, close to WEA, it mostly responds to surface winds. In WEA, our results suggest that the role of the low-level wind flow is also essential for the low-level cloud cover ISV, even if the linear relationship is far stronger at interannual time-scale (Moron et al., 2023). We believe that the relationship is lowered due to opposing relationships with the low-level westerlies (see below).

The LTS is well-known to be positively related to stratiform cloud cover interannual variations (Hu et al., 2008; Klein & Hartmann, 1993; Sun et al., 2011; Wood & Bretherton, 2006), and as expected, LTS_WEA is indeed positively related to WEA_{isv} ($r = 0.45$ at zero lag), mimicking, with a weaker amplitude, the relationship found at interannual time-scale (Moron et al., 2023). This correlation is larger than the one found between WEA_{isv} and either t700_WEA ($r = 0.31$ when t700_WEA leads by one day) and t925 ($r = -0.21$ at zero lag). Moreover, the correlation between LTS_WEA and q850_WEA is relatively low (0.11 at zero lag, peaking at 0.19 when LTS_WEA leads by one day), suggesting that both indices are involved through different processes (Figure 12).

We also include u925_WEA, despite its relatively low correlation with WEA_{isv} at zero lag ($r = 0.19$, and -0.19 when u925_WEA leads WEA_{isv} by two days). We hypothesise that the intraseasonal linear relationship between u925_WEA and WEA_{isv} is decreased versus the interannual time-scale (Moron et al., 2023), because increased westerlies lead to a conflicting forcing upon WEA_{isv}: u925_WEA strongly drives q850_WEA ($r = -0.52$ with a one-day lag, Figure 11) and is negatively related to both t925_WEA ($r = -0.60$) and t850_WEA ($r = -0.56$) at zero lag, in the sense that increased westerlies convey dry and cool air from the Atlantic. It agrees with findings by Schuster et al. (2013) established for the Guinean coast. So anomalous westerlies over WEA are positively related to WEA_{isv} because they convey cold air, increasing LTS_WEA ($r = 0.37$ at zero lag), but are negatively related to WEA_{isv} due to advection of drier air from the Atlantic.

We also noticed a switch between easterlies and westerlies around day 0 over WEA in Figures 3 and 4. This behaviour may be partly related to the loop enclosed by a dashed green line in Figure 13 and illustrating a negative feedback in a sequence of 3–5 days: anomalously strong low-level westerlies (u925_WEA) drive increased convection over the Congo Basin (OLR_CONG), which decreases the temperature over the Congo Basin (t925_CONG), probably in relation with the advection of the cool Atlantic air and the increased cloudiness related to deep convection: this cooling decreases the geopotential zonal gradient between CT and CONG (dz925 CT-CONG), which is positively related to u925_WEA, i.e., a cooling over the Congo basin leading to an easterly anomaly over WEA, thus reverting the initial westerly anomaly (Figure 13). Therefore, the ± switch seen with high-pass-filtered variations (Figure S9) is not a simple artefact of the high-pass filtering.

We should also remember that KW is a possible driver of this switch as suggested by Figure 10, and also because the time-scale revealed by Figure 13 is consistent with the one of KW. The association between KW and low-cloud cover is intriguing, since the Kelvin-filtered variance of brightness temperature (i.e., a proxy for convection) is relatively low over Africa in JAS, and especially modest outside the climatological location of the ITCZ (Mekonnen et al., 2008; Nguyen & Duvel, 2008). Nevertheless, the space–time pattern of the geopotential and low-level wind anomalies related to KW revealed by Mounier et al. (2007) and Mekonnen et al. (2008) in boreal summer are roughly consistent with our Figure 10. As seen in Figure S10, the fraction of variance explained by KW over Central Africa peaks over the central Congo Basin, mostly for zonal wind and temperature. When we look at the atmospheric indices selected in Figure 13, the KW (strong KW) explain 8.5%, 13.9% and 16.2% (respectively 18.4%, 24% and 28.9%, which is the maximum for all atmospheric indices analysed in this study) of the variance of u925_WEA, t925_CONG and OLR_CONG (the corresponding fractions of variance for WEA_{isv} and for u925_CT are respectively only 1.7% and 3.9% on one hand, and 3.7% and 8.1% on the other hand). Due to the seasonal latitudinal shift of the ITCZ, the

occurrence of strong KW close to the ITCZ over Central Africa peaks in June (24 days by mean) and is lower in July (18 days by mean) and August (17 days in mean). Based on the loop defined in Figure 13, we simply counted the frequency of cases when u925_WEA switches its sign three days after a given day. This represents in mean around 49% of the time and slightly increases to 54% when a strong KW occurs. So, KW may be a significant driver of the switching between easterly and westerly, partly related to OLR variations over the central Congo Basin (Ayesiga et al., 2022; Mekonnen et al., 2020; Zebaze et al., 2015), but this switching mode may also occur independently of KW, as explained above.

The other mechanisms shown in Figures 13 and 14 are merely linked to Rossby waves in the southern subtropical Atlantic, mostly operating at longer time-scales than 10 days. Two paths could be hypothesised. The first one links an increased dZ300 to an anomalous subsidence over WEA, NEQ and CONG (not shown) areas three days later. This increased subsidence drives a warming at 700 hPa one day later in the three sectors, in particular over WEA (Figure 13) and NEQ (not shown). The increased subsidence over NEQ drives an easterly (and northerly, not shown) anomaly at 700 and 850 hPa, thus advecting warm and moist air above and at the top of the stratiform cloud cover over WEA (Figure 13). We did not explore further the link between u850_NEQ and an easterly wave travelling over the eastern Sahel and Sudanian belt, but this may be an additional driver of moist and warm air supply to WEA (Berger et al., 2025). This anomalously warm and moist air may both increase LTS and thicken the cloud cover from its top.

The second path operates near the surface. A positive anomaly of dZ300 intensifies shortly the St. Helena anticyclone, which cools down the BEN area (Figure 11) through enhanced southerly winds, increased evaporation and increased vertical mixing with subsurface waters, while SCONG warms up ($r = 0.37$ when dZ300 leads t925_SCONG by three days). This thermal dipole is consistent with observations by Ward et al. (2021, 2023) of relationships between troughs over the Mediterranean sea and anomalous warming over the central to eastern Saharan–Sudanian belts in boreal winter. The weak cooling of SSTs over the SE Atlantic, then off WEA 4–6 days later (not shown), could also provide a relatively weak slow component to ISV. This delay between anomalous increased S–SE low-level winds and anomalous cooling over the equatorial Atlantic is consistent with the findings by de Coëtlogon et al. (2010, 2014). Of course, this relationship is far weaker than observed at interannual time-scale, where the dominant driver of low-cloud cover variations is related to SSTs over the cold-tongue area, through changes in the LTS and the intensity of downstream advection of Atlantic air through the W–SW low-level flow (Camberlin et al., 2023; Moron et al., 2023). At intraseasonal time-scale, the anomalous zonal thermal gradient between BEN and CONG may be also sustained through the cooling of the SE and equatorial Atlantic and the corresponding increase of southerlies over BEN ($r = -0.65$ between t925_BEN and v925_BEN at zero lag). The anomalous cooling over BEN drives anomalous easterlies over the CT area one day later, thus allowing it to enter the subequatorial loop described above (Figure 13). Again, the impact of this path upon WEA_{isv} is a priori ambiguous, since increased dZ300 leads, at the end, to anomalous easterlies over CT and WEA areas 3–4 days later, inducing a decreased stratiform cloud cover at zero lag (Figure 13). But, again, the relationship could be understood as the fact that anomalous easterlies over WEA precede an increase of WEA_{isv}.

5 | CONCLUSION

The intraseasonal variability of the stratiform cloud cover over WEA during the cloudiest season (i.e., JJAS) is investigated here using SYNOP observations (combining various sources and primarily based on the EECRA dataset; Aellig et al., 2022; Champagne et al., 2023) and ERA5 reanalysis data. The space–time variability of the stratiform cloud cover is synthesised into a standardised index blending observed and ERA5 low-level cloud fraction over the cloudiest area of WEA (i.e., coastal plains and windward slopes, plus Chaillu mountains of Gabon and SW Republic of Congo). The intraseasonal index does not show any clear, sharp and recurrent periodicity; the temporal variance is distributed over a broad bandwidth with a large variability across the years, so that each seasonal WEA_{isv} time series can be assimilated to a red-noise process. This aperiodic and noisy character may be, at least partly, induced by uncertainties related to small-scale variations of the low-level cloud cover, as well as errors/biases in the recording of the cloudiness. It suggests also that the ISV of the low-level cloud cover may not be entirely driven by periodic phenomena such as tropical waves, but are rather driven by different, and not necessarily related, phenomena operating on a broad bandwidth.

The first process revealed is related to a zonal dynamics linking the intensity of low-level westerlies and the zonal geopotential gradient between the cold-tongue area and the Congo Basin on one hand, and the intensity of deep convection over the Congo Basin on the other. In summary, more intense convection over the Congo Basin lags faster westerlies over WEA, but leads to an in-situ cooling over the Congo Basin, then weakening the geopotential gradient between the Congo Basin and the cold-tongue area,

and lastly the westerlies over WEA 3–5 days later. The key driver seems to be the intensity of deep convection over the Congo Basin. This zonal mode leads to counteracting signals on the stratiform cloud cover over WEA, related to increased low-level westerlies, between a higher LTS and a reduced content of moisture at low levels. This zonal mode could either be internally driven or triggered by KW, which promote a switch of zonal wind anomalies over WEA and the Congo basin.

Another important mechanism relates to the amount of moisture advected near the top of the stratiform cloud deck. Above 825 hPa, the mean flow is easterly in JJAS so that sources of moisture are located upstream of WEA, that is south of the African rainbelt and over the Congo Basin itself. Anomalous advection of moisture toward WEA at 850 hPa could be related to either a travelling easterly wave over the eastern Sahelian–Sudanian belt or an anomalous subsidence to the northeast of WEA.

Such anomalous subsidence may be driven by a Rossby wave dispersion from the extratropical South Atlantic. A near-standing Rossby wave associating an anomalous ridge over the SE South Atlantic and trough over southern Africa intensifies the St. Helena anticyclone system and the related low-level winds, including southerlies over the Benguela area, and enhances the thermal and geopotential gradients between the South Atlantic and southern Africa. Anomalous warming is also observed in the middle troposphere over equatorial Africa and the Guinean belt a few days after the peak amplitude of the Rossby wave. These features lead to increased low-cloud cover over WEA nearly 6–8 days later.

This study shows that ISV of the low-cloud cover over WEA is clearly more complex than the diurnal (Champagne et al., 2023; Dommo et al., 2018, 2022) and interannual variations (Moron et al., 2023). The combination of various mechanisms operating at different time-scales, and not necessarily periodic themselves, may explain the aperiodic character of the ISV of the low-cloud cover. Aperiodic variations do not exclude a significant, but partial and intermittent, role played by a quasi-periodic phenomenon such as KW. The complex variability is also related to conflicting mechanisms involving specific variables. The most obvious example is the role of the low-level in-situ westerlies, which advect cool, but dry, Atlantic air toward WEA. At the interannual time-scale, the thermal effect is clearly dominant (i.e., anomalously cold SST off WEA are associated with a cloudier season than usual; Moron et al., 2023), while it is far from being obvious at the intraseasonal time-scale analysed here. The anomalous advection of moisture near the top of, and above, the cloud cover seems to be at least as important as the temperature of the boundary layer. Some important drivers are also distant from WEA, as the Rossby waves travelling over the extratropical South Atlantic, and this long distance may blur the associated impact on the ISV. More generally, our study contributes to the analysis of the ISV over the Congo Basin. It will be interesting to further deepen the characteristics and relevance of the zonal mode which involves deep convection over the Congo Basin. Such a complex interaction between lagged multiscale phenomena, operating at different time-scales, and acting on a relatively noisy field as low-cloud cover, would certainly benefit from integrated approaches as causal inference networks (Runge et al., 2019).

ACKNOWLEDGEMENTS

We thank the reviewers for their comments and suggestions which helped us to clarify our initial manuscript. This study is part of the project 'Dynamics, Variability and Bioclimatic Effects of Low Clouds in Western Central Africa' (DYVALOCCA, https://dyvalocca.osug.fr/) funded by the French Agence Nationale de la Recherche (ANR) and the German Deutsche Forschungsgemeinschaft (DFG) from January 2020 to June 2023 under contracts ANR- 19-CE01-0021 and DFG FI 786/5-1, respectively. This work is also part of the International Joint Laboratory 'Dynamics of land ecosystems in Central Africa in a context of global changes' of the Institut de Recherche pour le Développement (LMI DYCOFAC IRD, https://www.lmi-dycofac.org/).

DATA AVAILABILITY STATEMENT

The three-hourly dataset of the 26 stations is available from Aellig et al. (2022). The ERA5 data have been extracted from the Copernicus data store (https://cds.climate.copernicus.eu). The OLR data have been extracted from the NOAA web site (https://psl.noaa.gov/data/gridded/data.olrcdr.interp.html).

ORCID

Vincent Moron https://orcid.org/0000-0002-4981-9530
Andreas H. Fink https://orcid.org/0000-0002-5840-2120
Peter Knippertz https://orcid.org/0000-0001-9856-619X

REFERENCES

Adebiyi, A.A. & Zuidema, P. (2018) Low cloud cover sensitivity to biomass-burning aerosols and meteorology over the southeast Atlantic. *Journal of Climate*, 31, 4329–4346.

Aellig, R., Moron, V., Camberlin, P., Champagne, O., Philippon, N., Fink, A.H. et al. (2022) Cloud observing data of 85 stations in western Central Africa. https://doi.org/10.5445/IR/1000150635

Andersen, H., Cermak, J., Fuchs, J., Knippertz, P., Gaetani, M., Quinting, J. et al. (2020) Synoptic-scale controls of fog and low-cloud variability in the Namib Desert. *Atmospheric Chemistry and Physics*, 20, 3415–3438.

Ayesiga, G., Holloway, C.E., Williams, C.J., Yang, G.Y., Stratton, R. & Roberts, M. (2022) Linking equatorial African precipitation to

kelvin wave processes in the CP4-Africa convection-permitting regional climate simulation. *Journal of the Atmospheric Sciences*, 79, 1271–1289.

Berger, A., Camberlin, P., Pergaud, J., Bahuet-Bourret, Y., Aellig, R., & Champagne, O. (2025) The dry-season low-level cloud cover over Western equatorial Africa: a case study with a mesoscale atmospheric model. *Quarterly Journal of the Royal Meteorological Society*. In press.

Camberlin, P., Togbedji, C.F., Pergaud, J., Berger, A., Aellig, R., Fink, A.H. et al. (2023) The representation of dry-season low-level clouds over Western equatorial Africa in reanalyses and historical CMIP6 simulations. *Climate Dynamics*, 61, 2815–2837.

Champagne, O., Aellig, R., Fink, A.H., Philippon, N., Camberlin, P., Moron, V. et al. (2023) Climatology of low-level clouds over Western equatorial Africa based on ground observations and satellites. *Journal of Climate*, 36, 4289–4306.

de Coëtlogon, G., Leduc-Leballeur, M., Meynadier, R., Bastin, S., Diakhaté, M., Eymard, L. et al. (2014) Atmospheric response to sea-surface temperature in the eastern equatorial Atlantic at quasi-biweekly time-scales. *Quarterly Journal of the Royal Meteorological Society*, 140, 1700–1714.

de Coëtlogon, G.D., Janicot, S. & Lazar, A. (2010) Intraseasonal variability of the ocean – atmosphere coupling in the Gulf of Guinea during boreal spring and summer. *Quarterly Journal of the Royal Meteorological Society*, 136, 426–441.

Dommo, A., Philippon, N., Vondou, D.A., Sèze, G. & Eastman, R. (2018) The June–September low cloud cover in Western Central Africa: mean spatial distribution and diurnal evolution, and associated atmospheric dynamics. *Journal of Climate*, 31, 9585–9603.

Dommo, A., Vondou, D.A., Philippon, N., Eastman, R., Moron, V. & Aloysius, N. (2022) The ERA5's diurnal cycle of low-level clouds over Western Central Africa during June–September: dynamic and thermodynamic processes. *Atmospheric Research*, 280, 106426.

Dyer, E.L.E., Jones, D.B., Nusbaumer, J., Li, H., Collins, O., Vettoretti, G. et al. (2017) Congo Basin precipitation: assessing seasonality, regional interactions, and sources of moisture. *Journal of Geophysical Research-Atmospheres*, 122, 6882–6898.

Eastman, R., Warren, S.G. & Hahn, C.J. (2011) Variations in cloud cover and cloud types over the ocean from surface observations, 1954–2008. *Journal of Climate*, 24, 5914–5934.

Ebisuzaki, W. (1997) A method to estimate the statistical significance of a correlation when the data are serially correlated. *Journal of Climate*, 10, 2147–2153.

Fuchs, J., Cermak, J. & Andersen, H. (2018) Building a cloud in the southeast Atlantic: understanding low-cloud controls based on satellite observations with machine learning. *Atmospheric Chemistry and Physics*, 18, 16537–16552.

Gu, G. & Adler, R.F. (2004) Seasonal evolution and variability associated with the west African monsoon system. *Journal of Climate*, 17, 3364–3377.

Gu, G., Adler, R.F., Huffman, G.J. & Curtis, S. (2004) African easterly waves and their association with precipitation. *Journal of Geophysical Research – Atmospheres*, 109, D04101.

Hahn, C.J., Warren, S.G. & Eastman, R. (2003) Cloud climatology for land stations worldwide, 1971–1996. Tech. Rep. NDP-026D, Carbon Dioxide Information Analysis Center, 35.

Hart, N.C., Washington, R. & Maidment, R.I. (2019) Deep convection over Africa: annual cycle, ENSO, and trends in the hotspots. *Journal of Climate*, 32, 8791–8811.

Hersbach, H., Bell, B., Berrisford, P., Hirahara, S., Horányi, A., Muñoz-Sabater, J. et al. (2020) The ERA5 global reanalysis. *Quarterly Journal of the Royal Meteorological Society*, 146, 1999–2049.

Hu, Z.Z., Huang, B. & Pegion, K. (2008) Low cloud errors over the southeastern Atlantic in the NCEP CFS and their association with lower-tropospheric stability and air-sea interaction. *Journal of Geophysical Research – Atmospheres*, 113, D12114.

Janicot, S., Lafore, J.P. & Throncroft, C. (2011) The west African monsoon. In: *The global monsoon system, Volume 5 of World Scientific Series on Asia-Pacific weather and climate*. Singapore: Word Scientific, pp. 111–135.

Janicot, S., Moron, V. & Fontaine, B. (1996) Sahel droughts and ENSO dynamics. *Geophysical Research Letters*, 23, 515–518.

Katz, R.W. & Glantz, M.H. (1986) Anatomy of a rainfall index. *Monthly Weather Review*, 114, 764–771.

Kiladis, G.N., Wheeler, M.C., Haertel, P.T., Straub, K.H. & Roundy, P.E. (2009) Convectively coupled equatorial waves. *Reviews of Geophysics*, 47, RG2003.

Klein, S.A. & Hartmann, D.L. (1993) The seasonal cycle of low stratiform clouds. *Journal of Climate*, 6, 1587–1606.

Liebmann, B. & Smith, C.A. (1996) Description of a complete (interpolated) outgoing longwave radiation dataset. *Bulletin of the American Meteorological Society*, 77, 1275–1277.

Lohou, F., Kalthoff, N., Adler, B., Babić, K., Dione, C., Lothon, M. et al. (2020) Conceptual model of diurnal cycle of low-level stratiform clouds over southern West Africa. *Atmospheric Chemistry and Physics*, 20, 2263–2275.

Magnan, M., Philippon, N., Moron, V., Mariscal, A. & Liandrat, O. (2024) Diurnal changes in cloud cover in eastern Gabon and their impacts on energy balance, light Availability, and water demand: a case study of the 2022 dry season. *Journal of Applied Meteorology and Climatology*, 63, 1445–1461.

Mekonnen, A., Schreck, C.J., III & Enyew, B.D. (2020) The impact of kelvin wave activity during dry and wet African summer rainfall years. *Atmosphere*, 11, 568.

Mekonnen, A., Thorncroft, C.D., Aiyyer, A.R. & Kiladis, G.N. (2008) Convectively coupled kelvin waves over tropical Africa during the boreal summer: structure and variability. *Journal of Climate*, 21, 6649–6667.

Moron, V., Camberlin, P., Aellig, R., Champagne, O., Fink, A.H., Knippertz, P. et al. (2023) Diurnal to interannual variability of low-level cloud cover over western equatorial Africa in may–October. *International Journal of Climatology*, 43, 6038–6064.

Mounier, F., Kiladis, G.N. & Janicot, S. (2007) Analysis of the dominant mode of convectively coupled kelvin waves in the west African monsoon. *Journal of Climate*, 20, 1487–1503.

Nguyen, H. & Duvel, J.P. (2008) Synoptic wave perturbations and convective systems over equatorial Africa. *Journal of Climate*, 21, 6372–6388.

Osborn, T. J., Briffa, K. R. & Jones, P. D. (1997) Adjusting variance for sample-size in tree-ring chronologies and other regional mean timeseries. *Dendrochronologia*, 15, 89–99.

Philippon, N., Cornu, G., Monteil, L., Gond, V., Moron, V., Pergaud, J. et al. (2019) The light-deficient climates of western central African evergreen forests. *Environmental Research Letters*, 14, 034007.

Philippon, N., De Lapparent, B., Gond, V., Sèze, G., Martiny, N., Camberlin, P. et al. (2016) Analysis of the diurnal cycles for a better

understanding of the mean annual cycle of forests greenness in Central Africa. *Agricultural and Forest Meteorology*, 223, 81–94.

Runge, J., Bathiany, S., Bollt, E., Camps-Valls, G., Coumou, D., Deyle, E. et al. (2019) Inferring causation from time series in earth system sciences. *Nature Communications*, 10, 2553.

Schlueter, A., Fink, A.H. & Knippertz, P. (2019b) A systematic comparison of tropical waves over northern Africa: part 2: influence on dynamics and thermodynamics. *Journal of Climate*, 32, 2605–2625.

Schlueter, A., Fink, A.H., Knippertz, P. & Vogel, P. (2019a) A systematic comparison of tropical waves over northern Africa: part 1: influence on rainfall. *Journal of Climate*, 32, 1501–1523.

Schuster, R., Fink, A.H. & Knippertz, P. (2013) Formation and maintenance of nocturnal low-level stratus over the southern west African monsoon region during AMMA 2006. *Journal of the Atmospheric Sciences*, 70, 2337–2355.

Sun, F., Hall, A. & Qu, X. (2011) On the relationship between low cloud variability and lower tropospheric stability in the Southeast Pacific. *Atmospheric Chemistry and Physics*, 11, 9053–9065.

Thorncroft, C.D. & Hoskins, B.J. (1994) An idealized study of African easterly waves. I: a linear view. *Quarterly Journal of the Royal Meteorological Society*, 120, 953–982.

van der Linden, R., Fink, A.H., Pinto, J.G., Phan-Van, T. & Kiladis, G.N. (2016) Modulation of daily rainfall in southern Vietnam during the southwest monsoon season by the madden-Julian oscillation and convectively coupled equatorial waves. *Journal of Climate*, 29, 5801–5820.

Verbeek, J.J., Vlassis, N. & Kröse, B. (2002) Coordinating principal component analyzers. In: Dorronsoro, J.R. (Ed.) *Artificial neural networks – ICANN 2002. ICANN 2002. Lecture notes in computer science*, Vol. 2415. Berlin, Heidelberg: Springer.

Ward, N., Fink, A.H., Keane, R.J., Guichard, F., Marsham, J.H., Parker, D.J. et al. (2021) Synoptic timescale linkage between midlatitude winter troughs Sahara temperature patterns and northern Congo rainfall: a building block of regional climate variability. *International Journal of Climatology*, 41, 3153–3173.

Ward, N., Fink, A.H., Keane, R.J. & Parker, D.J. (2023) Upper-level midlatitude troughs in boreal winter have an amplified low-latitude linkage over Africa. *Atmospheric Science Letters*, 24, e1129.

Washington, R., James, R., Pearce, H., Pokam, W.M. & Moufouma-Okia, W. (2013) Congo Basin rainfall climatology: can we believe the climate models? *Philosophical Transactions of the Royal Society, B: Biological Sciences*, 368, 1625.

Wood, R. (2012) Stratocumulus Clouds. *Monthly Weather Review*, 140, 2373–2423.

Wood, R. & Bretherton, C.S. (2006) On the relationship between stratiform low cloud cover and lower-tropospheric stability. *Journal of Climate*, 19, 6425–6432.

Zebaze, S., Lenouo, A., Tchawoua, C. & Janicot, S. (2015) Synoptic kelvin type perturbation waves over Congo basin over the period 1979–2010. *Journal of Atmospheric and Solar-Terrestrial Physics*, 130, 43–56.

SUPPORTING INFORMATION

Additional supporting information can be found online in the Supporting Information section at the end of this article.

How to cite this article: Moron, V., Camberlin, P., Philippon, N., Fink, A.H. & Knippertz, P. (2025) Regional to large-scale mechanisms controlling intraseasonal variability of low-level clouds in Western Equatorial Africa. *Quarterly Journal of the Royal Meteorological Society*, e4974. Available from: https://doi.org/10.1002/qj.4974